A&A, 703, A268 (2025)
https://doi.org/10.1051/0004-6361/202452213

Astronomy & Astrophysics

Identification and characterization of nascent planetary nebulae with OH and H_2O masers

Roldán A. Cala[1,⋆], José F. Gómez[1], Luis F. Miranda[1], Hiroshi Imai[2,3], Guillem Anglada[1], Itziar de Gregorio-Monsalvo[4], Keiichi Ohnaka[5], Olga Suárez[6], Daniel Tafoya[7], and Lucero Uscanga[8]

[1] Instituto de Astrofísica de Andalucía, CSIC, Glorieta de la Astronomía s/n, 18008 Granada, Spain
[2] Center for General Education, Comprehensive Institute of Education, Kagoshima University, 1-21-35 Korimoto, Kagoshima 890-0065, Japan
[3] Amanogawa Galaxy Astronomy Research Center, Graduate School of Science and Engineering, Kagoshima University, 1-21-35 Korimoto, Kagoshima 890-0065, Japan
[4] European Southern Observatory, 3107, Alonso de Córdova, Santiago de Chile, Chile
[5] Instituto de Astrofísica, Universidad Andrés Bello, Fernández Concha 700, Las Condes, Santiago, Chile
[6] Laboratoire Lagrange, UMR7293, Observatoire de la Côte d'Azur, Université Côte d'Azur, Boulevard de l'Observatoire CS 34229 06304 Nice Cedex, France
[7] Department of Space, Earth and Environment, Chalmers University of Technology, Onsala Space Observatory, 439 92 Onsala, Sweden
[8] Departamento de Astronomía, Universidad de Guanajuato, A.P. 144, 36000 Guanajuato, Gto., Mexico

Received 12 September 2024 / Accepted 18 September 2025

ABSTRACT

Stars such as the Sun expel their outer layers and form planetary nebulae (PNe) as they evolve into white dwarfs. PNe exhibit diverse morphologies, the origins of which are not fully understood. PNe with OH (OHPNe) and H_2O (H_2OPNe) masers are thought to be nascent PNe. However, the number of known OHPNe and H_2OPNe remains small, and only in eight cases has the position of the maser emission been found to coincide with the PN, using the high astrometric accuracy of interferometric observations. In order to identify more OHPNe and H_2OPNe, we used public databases and our own ATCA/VLA observations to match the positions of OH and H_2O masers with known PNe and radio continuum emitters, considering radio continuum emission as a possible tracer of the photoionized gas that characterizes PNe. Here we report the confirmation of positional coincidence of maser emission with one more PN, and 12 PN candidates. Moreover, we have confirmed three evolved stars as 'water fountains' (WFs) hosting H_2O masers. These WFs are associated with radio continuum emission, but their possible nature as PNe has not yet been confirmed. Although a final characterization of maser-emitting PNe as a group still requires confirmation of more objects, their distribution in the infrared color-color diagrams suggests that they are a heterogeneous group of PNe. In particular, the new OHPN IRAS 07027−7934 has been reported to contain a late [WC]-type central star, while the maser emission implies an O-rich envelope. This property is found in only one other known maser-emitting PN, although we found evidence that other confirmed and candidate OHPNe may also have mixed chemistry, since they show emission from polycyclic aromatic hydrocarbons. The new WF IRAS 18443−0231 shows radio continuum that is dominated by strong and variable non-thermal emission, as in magnetized outflows.

Key words. masers – astronomical databases: miscellaneous – stars: winds, outflows – planetary nebulae: general – infrared: stars – radio continuum: stars

1. Introduction

The morphology of low- and intermediate-mass stars with initial masses (M_i) up to $8\,M_\odot$ changes at the end of their life, when the spherical envelopes created during the asymptotic giant branch (AGB) phase somehow transform into the elliptical, bipolar, multipolar, and, in general, non-spherical forms of planetary nebulae (PNe; Manchado et al. 1996), which are nebulae photoionized by a hot central star that evolves towards a cooling white dwarf. Consequently, these hot central stars are expected to contain essential information for understanding the complete evolution of PNe. For example, the formation of circumstellar envelopes that are rich in oxygen (O) around central stars rich in carbon (C) (Zijlstra et al. 1991; Miranda et al. 2021) would be better understood by studying sources at the onset of this evolutionary phase.

⋆ Corresponding author: rcala@iaa.es

Maser emission has been considered as a tracer of nascent PNe (Zijlstra et al. 1989). In fact, masers of circumstellar nature are widespread in the AGB phase, but they seem to be extremely rare among PNe. During the AGB phase, the circumstellar envelope grows as the star loses mass at a rate of up to $\simeq 10^{-5}\,M_\odot\,yr^{-1}$, depending on the initial mass of the star (Decin et al. 2019). If the envelope is O-rich, special physical conditions can pump maser emission from molecules of SiO, H_2O, and OH (e.g. Reid & Moran 1981), but if it is C-rich, HCN and SiS masers are observed (e.g. Menten et al. 2018). Spatially resolved observations show that O-bearing masers in spherically symmetric AGB envelopes are stratified, with SiO, H_2O, and OH masers typically located at approximately 10, 100 and 1000 au, respectively (e.g. Reid & Moran 1981; Elitzur 1992; Diamond et al. 1994).

The intense mass-loss during the AGB removes a significant part of the mass of the star until the beginning of the post-AGB phase. During this post-AGB phase, the mass-loss rate drops to

10^{-8} $M_\odot$ yr^{-1} (Blöcker 1995b), the envelope gets detached from the star (Vassiliadis & Wood 1994; Miller Bertolami 2016) and then cools and expands. Favorable conditions for maser emission start to disappear, persisting up to 10, 10^2, and 10^3 yr after the beginning of the post-AGB phase for SiO, H_2O, and OH molecules, respectively (Lewis & Araújo 1989; Gómez et al. 1990). The central star shrinks and increases its effective temperature ($T_{\rm eff}$), until it reaches approximately ≃25 000–30 000 K, at which point it can photoionize the previously detached envelope and form a PN, 10^2–10^4 yr after the beginning of the post-AGB phase, depending on the initial mass of the star (Vassiliadis & Wood 1994; Miller Bertolami 2016). These timescales make circumstellar masers valuable signposts of nascent PNe. Moreover, soon after the beginning of the PN phase, the increasing number of ionizing photons from the hot central star starts to destroy these molecules, which may prevent the detection of maser emission in evolved PNe. On the other hand, dense molecular clumps, or an unknown special shielding mechanism, have been proposed to explain the presence of molecular masers after the onset of photoionization (Tafoya et al. 2007). Furthermore, the presence of thermal emission from some of these molecules in PNe, possibly due to dense condensations of material (e.g., Cox et al. 1998; Márquez-Lugo et al. 2013; Manchado et al. 2015), also indicates that they may survive on longer timescales (Schmidt & Ziuris 2019; Gold et al. 2024; Ouyang et al. 2024).

Therefore, the identification of maser-emitting PNe is extremely important because they could be a key to characterizing the beginning of the PN phase. So far, no PN has been found to host SiO masers (Cala et al. 2024a), and only in eight cases has H_2O and/or OH maser emission been confirmed to spatially coincide with the position of sources spectroscopically classified as PNe. These PNe associated with H_2O (H_2OPNe) or OH maser emission (OHPNe) may be among the youngest objects in this evolutionary phase. Most of them are bipolar nebulae, and the spatial distribution of the masers trace equatorial rings or toroidal structures close to the central star, although with two important exceptions. In K 3-35, the H_2O masers also trace the tip of bipolar jets (Miranda et al. 2001). In IRAS 15103−5754, the H_2O maser emission shows high-velocity components tracing a jet-like structure (Gómez et al. 2015b), which indicates that it is a 'water fountain' (WF). Similarly, OH masers have been observed tracing bipolar outflows of post-AGB stars (e.g., Zijlstra et al. 2001). The presence of masers in bipolar outflows of post-AGB stars and PNe means that this type of emission can arise not only from the remnants of maser-emitting regions from the AGB phase, but also that they can trace non-spherical mass-loss episodes.

The jet traced by H_2O masers in IRAS 15103−5754 mentioned above deserves further attention, since most WFs seem to be binary or multiple systems hosting a post-AGB star (Gómez et al. 2017; Khouri et al. 2021), whereas this source is the only WF that seems to host a PN (Gómez et al. 2015b). WFs can be defined, in general terms, as evolved stars whose H_2O maser emission traces collimated ejections. They have been classically identified by their large velocity range covered by the emission (up to hundreds of $km\,s^{-1}$; e.g., Imai et al. 2002; Gómez et al. 2011; Uscanga et al. 2023; Imai et al. 2023), larger than the ≳50 $km\,s^{-1}$ ranges expected by the spherical mass-loss, which builds up large-scale ($\geq 10^4$ au) slowly expanding envelopes (expansion velocities ≲25 $km\,s^{-1}$, typically traced by OH masers) during the AGB phase (te Lintel Hekkert et al. 1991). The spatial distribution and proper motions of the maser emission clearly show the presence of jets (e.g. Suárez et al. 2009; Orosz et al. 2019). In addition to these 'classical' WFs, there are other objects in which the velocity range of the H_2O maser spectra is relatively narrow ≲50 $km\,s^{-1}$, but some components fall outside the range covered by the OH maser emission, suggesting the presence of non-spherical mass loss (Gómez et al. 1994; Engels 2002). When observed with high angular resolution, the H_2O maser emission in these objects seem also to trace jets (e.g., Boboltz & Marvel 2005), so they can be considered as 'low-velocity' WFs. While the difference between classical and low-velocity WFs has been sometimes interpreted as a projection effect (Boboltz & Marvel 2005; Vlemmings et al. 2014), there is some evidence of evolution in the jet velocities of WFs, with slower ones being present closer to the beginning to the post-AGB phase (Yung et al. 2013). This possible evolutionary effect make WFs relevant also in the context of nascent PNe. Considering that the kinematical ages of WFs (∼10^2 yr; e.g., Day et al. 2010; Yung et al. 2011; Orosz et al. 2019) are similar to the timescales of disappearance of H_2O maser emission after the AGB phase, a potential group of PNe with WF characteristics should be extremely rare and probably at the onset of photoionization.

The central stars of H_2OPNe and OHPNe are heavily obscured at optical wavelengths, and only in two cases has a stellar classification been proposed. In IRAS 18061−2505, the central star shows broad carbon emission lines and has been classified as [WC8] (see Miranda et al. 2021, and references therein), implying that it is C-rich. In Vy 2-2, Arkhipova et al. (2017) suggested the presence of weak stellar emission lines (*wels*) similar to those observed in other central stars (see Tylenda et al. 1993; Marcolino & Araujo 2003; Weidmann et al. 2020), although *wels* may not be a real spectral type (see Parthasarathy et al. 1998; Weidmann et al. 2015). With these few cases, it is impossible to assert whether maser-emitting PNe are associated with a particular type of central star or whether they are a common phase of different types of central stars at the beginning of the PN phase. Therefore, it is essential to identify more H_2OPNe and OHPNe to understand the nature and evolution of these objects.

2. Procedure to search for new maser-emitting PNe

In order to find new maser-emitting PNe, there are two different aspects to tackle. The first is to ensure that the maser emission is actually associated with a prospective PN. This is the main focus of this paper. The second is to determine whether the maser-emitting source is actually a PN, rather than another type of object.

Regarding the spatial location of the maser emission, many searches for maser emission toward evolved stars are carried out with single-dish telescopes, which typically have beam sizes of several arcminutes. For example, the Green Bank Telescope, one of the largest radio telescopes in the world (100 m diameter), has a half-power beam size of ≃30″ at 22 GHz (for H_2O masers) and ≃8′ at 1.6 GHz (for OH masers). When the spectrum is obtained with a single-dish antenna only at the catalog position of the source, the detected maser emission can arise from any source within that beam and, if the contaminant maser is strong enough, the emission can even spill through the antenna sidelobes (cf. the case of IRAS 19071+0857 in Gómez et al. 2015a), significantly farther away than the nominal beam width at half maximum. It is possible to improve the positional accuracy of a single-dish observation, by taking several spectra offset from the nominal

position of the source and fitting the decrease of emission assuming that the beam has a Gaussian profile. The astrometric error in this case is determined by the antenna rms pointing accuracy (which is typically several arcseconds) and the Gaussian profile fitting error (1σ error $\simeq\theta/(2\times \mathrm{snr})$, where θ is the telescope beam, and snr is the signal-to-noise ratio of the maser spectrum), which can also amount to several arcseconds, even with a good signal-to-noise ratio. The resulting theoretical astrometric accuracy of tens of arcseconds in single-dish observations may not even be enough to ascertain whether the emission arises from our target of interest, especially in crowded fields, such as the Galactic Bulge. Moreover, observing a maser source with different angular offsets is rarely done in maser surveys, since it is very time-consuming and, therefore, the positional uncertainty for detections in these surveys is of the order of arcminutes. Hence, single-dish reports of maser emission are usually not accurate enough to determine the location of the emitting source. In some particular cases, the probability that the emission seen with a single-dish telescope arises from a contaminant source within the beam may be low, specially when observing at high galactic latitudes, or if the velocity of the maser emission is close to the central velocity of the target source obtained with line observations at other frequencies. In the case of OH masers, a strong infrared source is required for their excitation. While H_2O masers do not necessarily require a strong infrared source, H_2OPNe often exhibit significant infrared excess due to their thick circumstellar envelopes. Therefore, if there is only a single strong infrared source within a single-dish beam, and the maser velocity is consistent with that of the star, there is little doubt on the identification of the maser-emitting source, especially in the case of OH emission. However, in general, radio interferometric observations with much higher positional accuracy are necessary for a definitive confirmation of the association of the maser emission with a PN (e.g. Miranda et al. 2001; Cala et al. 2024a).

In practice, our general strategy for finding new candidate maser-emitting PNe is to match the position of H_2O and OH masers and radio continuum emission, considering the latter as a tracer of the photoionized gas that characterizes PNe. Both maser and radio continuum emission can be observed with radio interferometers, which provide much improved positional accuracy over single-dish telescopes. The absolute astrometric accuracy in interferometers is determined by different factors, such as phase errors during the observations or how accurately the position of the antennas and the coordinates of the calibrators used for phase reference are known. The astrometric errors due to these factors amount to a fraction (roughly 10%) of the size of synthesized beam of the interferometers, so, in principle, it is relatively easy to achieve accuracies better than one arcsecond.

The best results can be achieved if the continuum observations are close in frequency to the maser lines, so they can be carried out simultaneously with the same telescope, sharing the same amplitude and phase calibration. In this case, the absolute astrometry is not so important for a spatial match between maser and continuum, but rather the relative positional errors between them, which is only determined by the signal-to-noise ratio of the emission (uncertainty $\simeq\theta/(2\times \mathrm{snr})$). These relative positional errors can reach values much smaller than the absolute astrometric precision for images with a high signal-to-noise ratio, and it is possible to spatially match maser and radio continuum emission with relative accuracies of a few milliarcseconds using interferometers with synthesized beams of $\simeq 1''$.

These extremely high relative accuracies between maser and continuum emission can provide further valuable information, such as the location of masers close to the central star, or on the nebular lobes (e.g., Miranda et al. 2001). Moreover, these accuracies also apply to the individual maser components, so it is possible to determine their spatial distribution, tracing structures such as toroids or jets.

After identifying prospective PN candidates by spatially matching radio continuum and maser emission, our second task is to confirm their nature as true PNe, since maser and radio continuum emission can both be present in objects that are not PNe, such as compact and ultracompact H II regions, post-AGB stars, galaxies, young stellar objects, symbiotic stars, supernova remnants and red nova remnants (e.g. Hofner & Churchwell 1996; Deguchi et al. 2005; Cho & Kim 2010; Qiao et al. 2016b, 2018, 2020; Ortiz-León et al. 2020, and references therein). The confirmation of an object as a PN requires additional observations, such as multiwavelength imaging and spectroscopy.

For this paper, we started by carrying out an extensive literature search, to identify new H_2O and OH maser-emitting PN candidates. To this end, we cross-matched sources in radio continuum surveys (e.g. Zoonematkermani et al. 1990; Helfand et al. 1992; Becker et al. 1994; Condon et al. 1998; White et al. 2005; Urquhart et al. 2009; Murphy et al. 2010; Purcell et al. 2013; Wang et al. 2018; Irabor et al. 2018; Medina et al. 2019; Gordon et al. 2021; Hale et al. 2021; Irabor et al. 2023; Dzib et al. 2023) with maser databases (e.g. Forster & Caswell 1989; Benson et al. 1990; Engels & Bunzel 2015; Ladeyschikov et al. 2019). We also matched the same maser databases with objects labeled as true, possible, and likely PNe in the Hong Kong/AAO/Strasbourg Hα (HASH) PN database (Parker et al. 2016).

The initial source list compiled after this search was subsequently purged, first by getting rid of bona fide PNe and PN candidates that have already been interferometrically confirmed in the literature as maser emitters (see Cala et al. 2022, and references therein), and of sources whose radio continuum emission is known to be associated with objects that are not evolved stars. In Table 1, we present the final sample of 29 confirmed or candidate PNe that may be associated with maser emission, resulting from our catalog matching and search of the literature.

Our list of sources can be classified, based on whether the association between maser and continuum emission has been confirmed with the high positional accuracy of interferometric observations (sources labeled as "I"), or if only single-dish maser observations have been reported (labeled as "S"), and whether the target has been previously confirmed as a PN (label "P"), or the nature of the radio continuum source is still unknown, and therefore, it is only a PN candidate (label "C"). Therefore, we can define four different categories of sources, with the following labels used in the seventh column of Table 1 (status):

1. SC: radio continuum sources of unknown nature within the beam of a single-dish maser detection.
2. SP: planetary nebulae within the beam of a single-dish maser detection.
3. IC: radio continuum sources whose association with maser emission has been confirmed interferometrically. In the following, we will refer to these sources as candidate maser-emitting PNe (candidate OHPNe and/or candidate H_2OPNe).
4. IP: planetary nebulae with interferometrically confirmed association with maser emission. We will refer to them as confirmed maser-emitting PNe (confirmed OHPNe and/or confirmed H_2OPNe).

Our initial search resulted in 11 SC, 10 SP, and eight IC.

In this paper, we have carried out interferometric observations of maser and radio continuum emission of sources labeled

Table 1. Initial sample of confirmed or possible maser-emitting PNe.

Name	Alt. name	Coordinates[a]		Maser emission[b]		Status[c]	References[d]		
		RA(J2000)	Dec(J2000)	H_2O	OH		H_2O	OH	Nature
IRAS 07027−7934	Vo 1	06:59:26.41	−79:38:47.0	ND	D	SP	1	2	3, 4
IRAS 14079−6402	WRAY 16-146	14:11:46.27	−64:16:24.0	–	D	SP	–	5	6
IRAS 14086−6907		14:12:50.43	−69:21:09.0	–	D	SC	–	5	7
IRAS 15559−5546	WRAY 16-198	15:59:57.63	−55:55:33.0	–	D	SP	–	5	8
IRAS 16029−5055	SCHD 68	16:06:40.63	−51:03:57.2	–	D	IC	–	9	10
IRAS 16280−4008	NGC 6153	16:31:30.57	−40:15:13.1	–	D	SP	–	11	12
IRAS 17180−2708	PN M 3-39	17:21:11.49	−27:11:37.9	–	D	SP	–	11	8
IRAS 17253−2824		17:28:30.68	−28:26:54.0	–	D	SC	–	5	13
IRAS 17374−2700		17:40:33.15	−27:02:25.3	–	D	SC	–	5	13
IRAS 17385−2211	PN M 3-13	17:41:36.60	−22:13:02.9	–	D	SP	–	5	13
PN H 2-18		17:43:28.75	−21:09:52.0	–	D	SP	–	5	14
IRAS 17487−1922	OH 008.9+03.7	17:51:44.92	−19:23:43.8	ND	D	SC	15	5	16
IRAS 18213−1245A		18:24:10.40	−12:43:22.8	D	D	IC	17	18	19
IRAS 18243−1048		18:27:08.24	−10:46:09.6	–	D	SC	–	5	20
IRAS 18271−1014		18:29:56.09	−10:12:12.9	–	D	SC	–	21	22
IRAS 18295−2510	NGC 6644	18:32:34.70	−25:07:45.7	–	D	SP	–	5	23
OH 25.646−0.003		18:38:06.14	−06:28:51.2	–	D	IC	–	18	24
IRAS 18464−0140	OH 31.21−0.18	18:48:56.66	−01:36:42.9	D	D	IC	25	25	19
IRAS 18443−0231	RFS 505	18:47:00.41	+00:12:29.8	D	–	SP	26	–	27, 28
IRAS 18480+0008		18:50:36.65	+00:12:29.8	–	D	IC	–	18	19
IRAS 18508+0047	GPSR5 33.906−0.044	18:53:22.10	+00:50:49.2	–	D	IC	–	18	19
IRAS 19035+0801	PM 1−279	19:05:56.40	+08:05:57.9	–	D	SC	–	29	30
IRAS 19123+1139		19:14:40.87	+11:44:49.3	–	D	SC	–	31	22
IRAS 19127+1717	SS 438	19:14:59.72	+17:22:46.0	ND	D	SP	32	33	34
IRAS 19176+1251	GLMP 898	19:19:55.77	+12:57:37.6	ND	D	IC	15	18	19
IRAS 19194+1548		19:21:40.46	+15:53:54.6	–	D	IC	–	18	19, 35
IRAS 19200+1035		19:22:26.80	+10:41:21.2	ND	D	SC	36	37	38
IRAS 19508+2659		19:52:57.86	+27:07:44.7	D	D	SC	39	40	41
IRAS 20266+3856		20:28:30.67	+39:07:01.2	ND	D	SC	31	42	41

Notes. [a] Position of the radio continuum emission reported in the literature, used as the phase center of our observations (Table A.1). [b] D: detected. ND: not detected. –: no observations available. [c] Source status, as defined in Section 2. [d]Reference for the maser emission (columns H_2O, OH). The last column (nature) indicates references that spectroscopically confirmed the sources with SP status as PNe. For PN candidates (SC, IC), that column reports the radio continuum detection: 1. Suárez et al. (2009). 2. Zijlstra et al. (1991). 3. Menzies & Wolstencroft (1990). 4. Surendiranath (2002). 5. te Lintel Hekkert et al. (1991). 6. Suárez et al. (2006). 7. Hale et al. (2021). 8. Frew et al. (2013). 9. Sevenster et al. (1997). 10. Irabor et al. (2023). 11. te Lintel Hekkert & Chapman (1996). 12. Pottasch et al. (1986). 13. Kimeswenger (2001) 14. Gesicki et al. (2024). 15. Gómez et al. (2015a). 16. Kohoutek (2001). 17. Walsh et al. (2014). 18. Beuther et al. (2019). 19. Wang et al. (2018). 20. Helfand et al. (1992). 21. Davis et al. (1993). 22. Urquhart et al. (2009). 23. Hsia et al. (2010). 24. White et al. (2005). 25. Forster & Caswell (1989). 26. Urquhart et al. (2011). 27. Cooper et al. (2013). 28. Kanarek et al. (2015). 29. Yung et al. (2013). 30. Van de Steene & Pottasch (1995). 31. Yung et al. (2014). 32. Yoon et al. (2014). 33. Likkel (1989). 34. Whitelock & Menzies (1986). 35. Sabin et al. (2014) 36. Benson et al. (1996). 37. Benson et al. (1990). 38. Zijlstra et al. (1989). 39. Cesaroni et al. (1988). 40. Eder et al. (1988). 41. Zoonematkermani et al. (1990). 42. te Lintel Hekkert et al. (1989).

as SC and SP in Table 1, to confirm whether both types of emission are spatially associated, so that we could update their status to IC or IP. We also observed the H_2O maser emission in the IC IRAS 19194+1548, to find out whether it is associated with this emission, in addition to OH maser one. We did not pursue observations of two ICs (IRAS 18213−1245A and IRAS 18464−0140), since that spatial association was already confirmed from interferometric data in the literature. However, these two sources are discussed in Appendix C, together with the sources for which our interferometric observations allow us to update them as either IP or IC.

Determining the evolutionary stage of an evolved star, particularly in the transition from the AGB to the PN phase, remains a complex and widely debated issue, especially in the absence of optical and infrared imaging and spectroscopy. In this context, establishing whether the sources presented in this paper as candidate PNe are genuine PNe (that is, an update from C to P status) is beyond the scope of this work. However, we discuss in Appendix C some of the available evidence that suggests a possible PN nature for some of our targets.

3. Observations and data processing

We observed 27 of the 29 sources (see above) of the initial sample listed in Table 1. Additionally, we observed the previously identified OHPNe candidates IRAS 17494−2645 and IRAS 18019−2216 (Cala et al. 2022) to search for H_2O maser emission. The observations were carried out with the Australia Telescope Compact Array (ATCA) of the Australia Telescope National Facility (ATNF) and the Karl G. Jansky Very Large Array (VLA) of the National Radio Astronomy Observatory (NRAO). Table A.1 shows the final list of observed targets, as well as the main parameters of our radio interferometric observations.

3.1. ATCA

ATCA observations (ID: C3390, PI: R.A. Cala) were carried out in two 12-hour sessions performed on 2020 October 19 and 20 using the 6A configuration of the telescope. The CFB 1M-0.5k mode of the Compact Array Broadband Backend (CABB) was configured to observe the ground level OH transitions at L band, with the rest frequencies 1612.2309, 1665.4018, 1667.3590, and 1720.5299 MHz, with a total bandwidth of 1 MHz each, sampled over 6146 channels of 0.5 kHz (total velocity coverage of 557 km s^{-1} and velocity resolution of ∼90 m s^{-1} for each line) and full linear polarization products. The velocity coverage is enough to detect the range of ∼120 km s^{-1}, which is the maximum range detected in OH in any of our target sources from single-dish observations. Also, the channel width is narrower than the reported linewidths. In both sessions, we observed continuum emission at an intermediate frequency centered at 2.1 GHz, with full linear polarization and a bandwidth of 2 GHz sampled into 2048 broadband channels. A second intermediate frequency replicates the same frequency configuration. The flux and bandpass calibrator in both observing sessions was PKS 1934-638. Variations in phase and amplitude were tracked by interleaving observations of our targets with nearby phase calibrators (Table A.1).

Manual flagging of bad data, as well as calibration of visibilities were performed with the MIRIAD software following standard data reduction procedures. For the continuum data, further flagging of the channels containing the frequencies of the ground-state OH maser transitions, as well as imaging of the calibrated visibilities, were done with the Common Astronomy Software Applications (CASA; CASA Team 2022) using tasks *plotms* and *tclean*, respectively. For the line data, spectral data cubes were obtained with the Astronomical Image Processing System (AIPS), since it proved to be significantly faster than CASA. First, we corrected the Doppler shift in the spectral line data due to the observatory motion to align the observations of each source with the same kinematical local standard rest (LSR) velocity ($V_{\rm LSR}$), using task *cvel* of AIPS. Imaging was performed using task *imagr*. Self-calibration was attempted on the channel with brightest OH maser emission, but we did not obtain a significant improvement in the signal-to-noise ratio (S/N) of any of the sources. We present data without applying self-calibration. In the detected sources we also tried to split the band of 2 GHz width into several subbands, to better sample the frequency dependence of flux density. However, the resulting emission either was not detected or had a very low S/N ratio. Thus, we report their continuum emission over the full bandwidth.

3.2. VLA

VLA observations (ID: 21A-138, PI: R.A. Cala) were carried out in the D configuration of the array, in four observing blocks (OBs) performed in 2021 March and April (see Table A.1). Two OBs were dedicated to L-Band (1–2 GHz) observations and the other two OBs to K-Band (20–24 GHz) observations. For the L band, the VLA correlator was configured with 8-bit samplers. This allowed us to observe the 1612.2309 MHz OH transition within a 4 MHz subband, sampled over 4098 channels (velocity coverage and resolution of ∼743 and ∼0.18 km s^{-1}, respectively), and the 1665.4018, 1667.3590, and 1720.5299 MHz OH lines, each with a 2-MHz wide subband sampled over 2048 channels (velocity coverage and resolution of ∼360 and ∼0.18 km s^{-1}, respectively). Sixteen additional subbands were set up to cover the whole 1 GHz provided by the 8-bit sampler, for continuum detection. For K band, the 8-bit and 3-bit samplers were mixed, in order to efficiently observe spectral line and radio continuum emission simultaneously. The 8-bit sampler was used to observe the 22235.08 GHz H_2O maser transition using a 32 MHz subband, sampled over 2048 channels (velocity coverage and resolution of ∼421 and ∼0.21 km s^{-1}, respectively). The velocity coverage is enough to detect the range of ∼68 km s^{-1}, which is the maximum velocity range detected of H_2O masers in any of our target sources from single-dish observations. The spectral resolution is finer than the reported linewidths. Moreover, 4 subbands of 128 MHz each (512 MHz in total) of the 8-bit sampler and the whole 4 GHz bandwidth of the 3-bit sampler pairs were dedicated for detection of continuum emission. The absolute flux calibrator was 3C286. The quasar J1733−1304 (QSO B1730−130) was used as a bandpass calibrator. Sources close to our targets in the sky were chosen as phase calibrators (Table A.1), to correct for phase and amplitude variations.

The continuum and line emission data of each OB was calibrated independently using the VLA pipeline implemented in CASA. After initial imaging with CASA, we tested self-calibration using the channels with brightest maser emission in each detected source. We were only successful in improving the S/N of the H_2O maser data of IRAS 18443−0231 and IRAS 18480+0008. Moreover, comparing our self-calibration results with CASA and AIPS, we noticed that the latter provided S/N ratio a factor of ∼1.4 times better than CASA in the channel with the most intense maser emission. Hence, we kept the successful self-calibration solutions obtained in AIPS for this channel, and applied them to the rest of the spectral line data and to all continuum spectral windows at K band for these two sources. Self-calibration of the continuum data of IRAS 17494−2645 and IRAS 19194+1548 also significantly improved the S/N of this emission. After self-calibration, subsequent imaging of both continuum and line emission was performed in CASA using the task *tclean*. As in the case of the ATCA data, to better sample the frequency dependence of flux density, we tried to split the data into different frequency ranges. We started with IRAS 18443−0231, which was the strongest source detected and, therefore, the one with the highest S/N. We split the bandwidth of band L and band K data in two different frequency ranges each. These values will be presented below in the discussion of spectral indices in Section 5.5. In the remaining sources, we noticed that the S/N of the resulting emission in the L band was very low and, in addition, the small relative frequency coverage of the K band around 22 GHz would not result in a significant improvement of their spectral indices reported in Section 5.5, at the expense of lowering an already limited S/N. Thus, for all sources except IRAS 18443−0231, we present only one value of flux density per observed band.

For sources IRAS 18443−0231, IRAS 18464−0140, and IRAS 18508+0047, we found and processed archival VLA data of continuum emission. For IRAS 18443−0231 we found VLA B configuration data from observations performed on January 10 2014 (ID: 13A-334, PI: K. Menten) which allowed us to create a continuum map of the emission at 5.7 GHz. For IRAS 18464−0140 and IRAS 18508+0047 we found archival VLA data from observations performed in the A configuration on March 08 2022 (ID: 22A-297, PI: A. Yang) which allowed us to create continuum emission maps at 10 GHz. All of these continuum data were processed with the VLA CASA pipeline, successfully self-calibrated, and imaged in CASA. Moreover, for IRAS 18464−0140 we reprocessed archival VLA H_2O maser data from observations performed with the C configuration on 21 June 1984 (ID: AF80, PI: J. R. Forster). The initial calibration of

these data was carried out with CASA. Self-calibration was successfully applied with AIPS using the channel with the brightest maser emission.

4. Results

The initial criterion, we have used to assess the interferometric association between the maser and the continuum emission is that the distance between the maser and the peak of the continuum emission is smaller than the FWHM synthesized beam of the continuum map, in the case of unresolved sources. This match criterion is the same as that used in previous searches of nascent PNe (e.g. Payne et al. 1988; Zijlstra et al. 1989; de Gregorio-Monsalvo et al. 2004; Uscanga et al. 2012). If the continuum emission of the target is resolved, then the criterion is that the maser emission falls within a four-sigma contour level of this resolved emission. We then carefully examined the sources with and without a positional match following these criteria, to minimize false positives and negatives.

In the case of identified possible matches, we have to rule out the possibility that the continuum and the maser emission may arise from different sources lying close in the sky. Most distances between the maser and continuum emission are less than 2″, which makes the chance of alignment highly unlikely. However, we inspected optical and infrared images to make sure that there is no obvious contaminant source near the main infrared source from which maser emission is most likely to arise. In some cases where we could determine the distribution of maser emission, this shows a morphology that aligns well with the elongation of the nebula traced by radio continuum emission, which further reinforces their mutual association. We therefore conclude that in all matches we found, the same object is the source of maser and radio continuum radiation.

In Table B.1, we show the interferometric positions of the radio continuum and maser emission of the matches we found, as well as the angular distance between the two types of emission (δ). In some cases, these spatial matches were obtained from the positions reported in literature data. Moreover, our interferometric ATCA/VLA observations allowed us to upgrade the status of several of the sources labeled SC or SP in Table 1 to either IC or IP. This updated status is also presented in Table B.1, with a different nomenclature that reflects the particular maser species involved. Details of these sources are presented in the Appendix C.

Spectra of the detected maser emission in our data are presented in Fig. 1. Our criterion for claiming a positive detection of a maser spot is that the emission is present above 3 sigma in at least three consecutive velocity channels and at a compatible position, which makes the probability of a false positive virtually negligible. In three objects, our positional accuracy was enough to determine the spatial distribution of the individual H_2O maser components. The parameters of these spectral components are listed in Appendix B.2. Maps of their spatial distributions are presented in Fig. 2. As mentioned in Appendix B.2, the positional uncertainties are those obtained with a fit of an elliptical Gaussian to the channel with the peak emission of each maser component. The radio continuum emission appears unresolved in all cases, except for IRAS 18443−0231 (Appendix C.2.3), where we can see some extended emission.

To minimize the possibility of false negatives, we also inspected images at different wavelengths of the sources for which the maser emission falls outside the beam of the continuum observations (for unresolved sources) or the total extent of the emission (for resolved sources). Our goal was to discard the fact that, despite their apparent misalignment, the maser and continuum emission may arise from different locations from the same source (e.g., the central star or the lobes in a PNe). After this analysis, we could discard as possible maser-emitting PNe several of the objects labeled as SC and SP in Table 1, since the maser and continuum emission appear associated with different sources. These are presented in Table B.9 and details of individual sources are given in Appendices B.3.1 to B.3.6. In the case of sources in which either maser or continuum emission was not detected in our data (Table B.10), we cannot confirm or discard a putative association, since variability could bring either emission below our sensitivity threshold.

5. Source characterization

After confirmation of the association between maser and radio continuum emission, we investigated whether the identified objects are consistent with being PNe. Although some of the sources in which we found an interferometric match between maser and continuum emission have been classified spectroscopically as PNe in the literature, no such classification is available for the ones we termed candidate maser-emitting PNe. In this section, we present some further characterization of all sources in Table B.1, which shows that all candidate sources seem to be evolved objects, rather than extragalactic sources or YSOs, source types which could also show maser and continuum emission. Therefore, all our candidate sources are compatible with being PNe, although in several cases further observations are necessary to determine whether the radio continuum emission arises from a photoionized region or from shock-ionized gas, as seen in post-AGB stars (e.g., Pérez-Sánchez et al. 2017).

5.1. Spectral energy distribution (SED)

We have collected all available archival optical, infrared, and millimeter data, together with the radio data presented in Section 5.5, to build their SED between ∼0.5 µm and 40 cm. Optical and infrared data were obtained from the Two Micron All Sky Survey (2MASS), AKARI, Deep Near Infrared Survey of the Southern Sky (DENIS), Gaia, *Herschel* Space Observatory, Infrared Astronomical Satellite (IRAS), Midcourse Space Experiment (*MSX*), Panoramic Survey Telescope and Rapid Response System (Pan-STARRS), Spitzer Space Telescope, United Kingdom Infrared Telescope (UKIRT), United States Naval Observatory (USNO)-B catalog, Visible and Infrared Survey Telescope for Astronomy variable survey (VVV), and Wide-field Infrared Survey Explorer (all-*WISE* survey). Flux densities at 3 mm were obtained from Ginsberg et al. (2020). These SEDs are presented in Fig. 3, with the exception of IRAS 17494−2645 and IRAS 18019−2216, which were already shown in Cala et al. (2022).

Although SEDs alone are not sufficient to unambiguously determine the nature of these objects, there are some useful trends that can give support to a prospective classification. The SEDs of all sources in this paper show significant similarities and, in particular, they present their emission peak at λ<60 µm. This feature is also observed in the SEDs of confirmed and candidate H_2OPNe and OHPNe previously reported (Uscanga et al. 2012; Cala et al. 2022) and, in general, it is also the case of compact PNe (Zhang & Kwok 1991), and optically obscured post-AGB stars and PNe (e.g. Ramos-Larios et al. 2009, 2012). Moreover, the shape of the SED and the wavelength of the peak is significantly different from other types of objects that present both maser and radio continuum

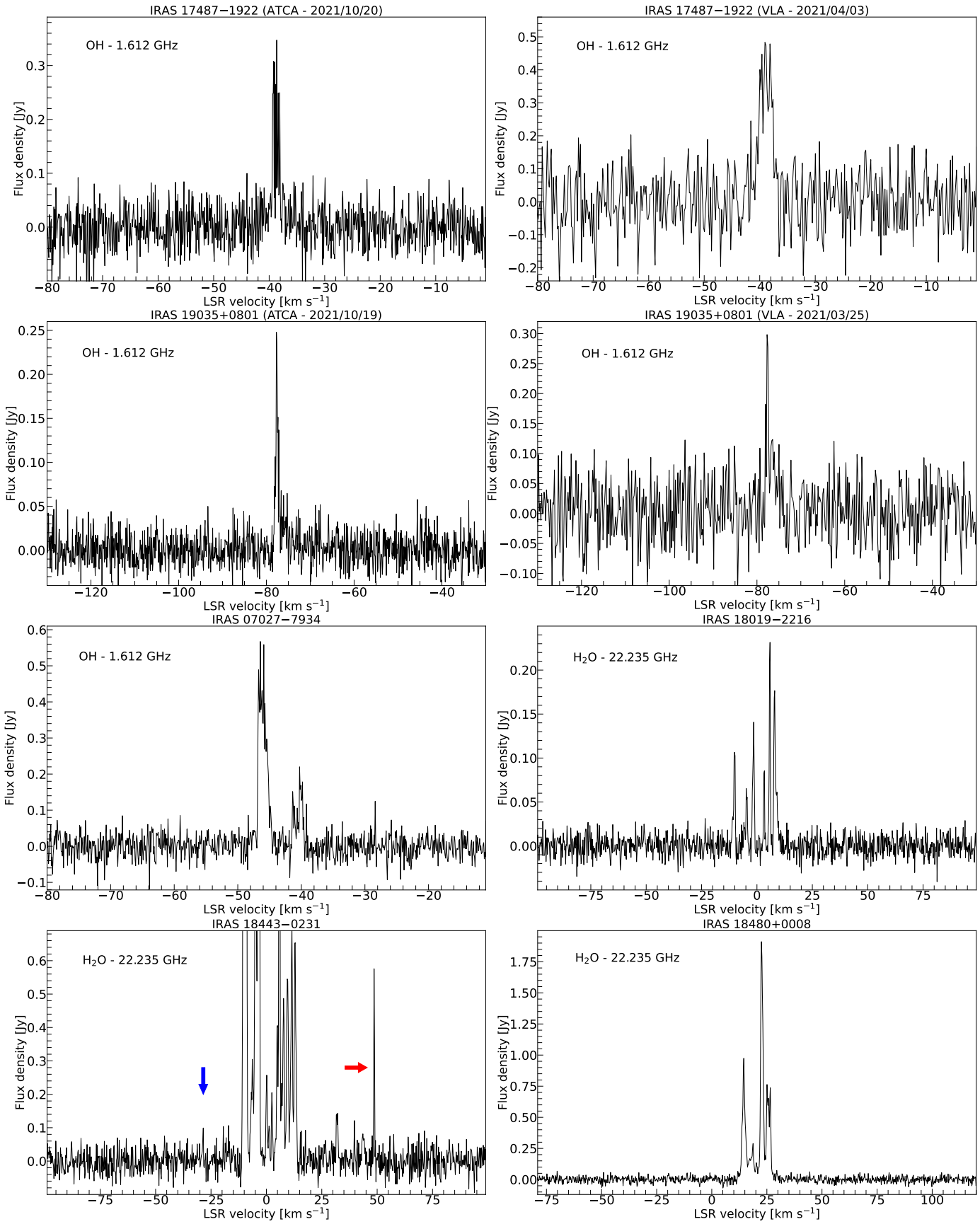

Fig. 1. Spectra of OH and H_2O emission detected in our observations. In IRAS 18443−0231 we show an enlarged view to clearly show the most blueshifted and redshifted H_2O masers, which are indicated by a blue and red arrow, respectively.

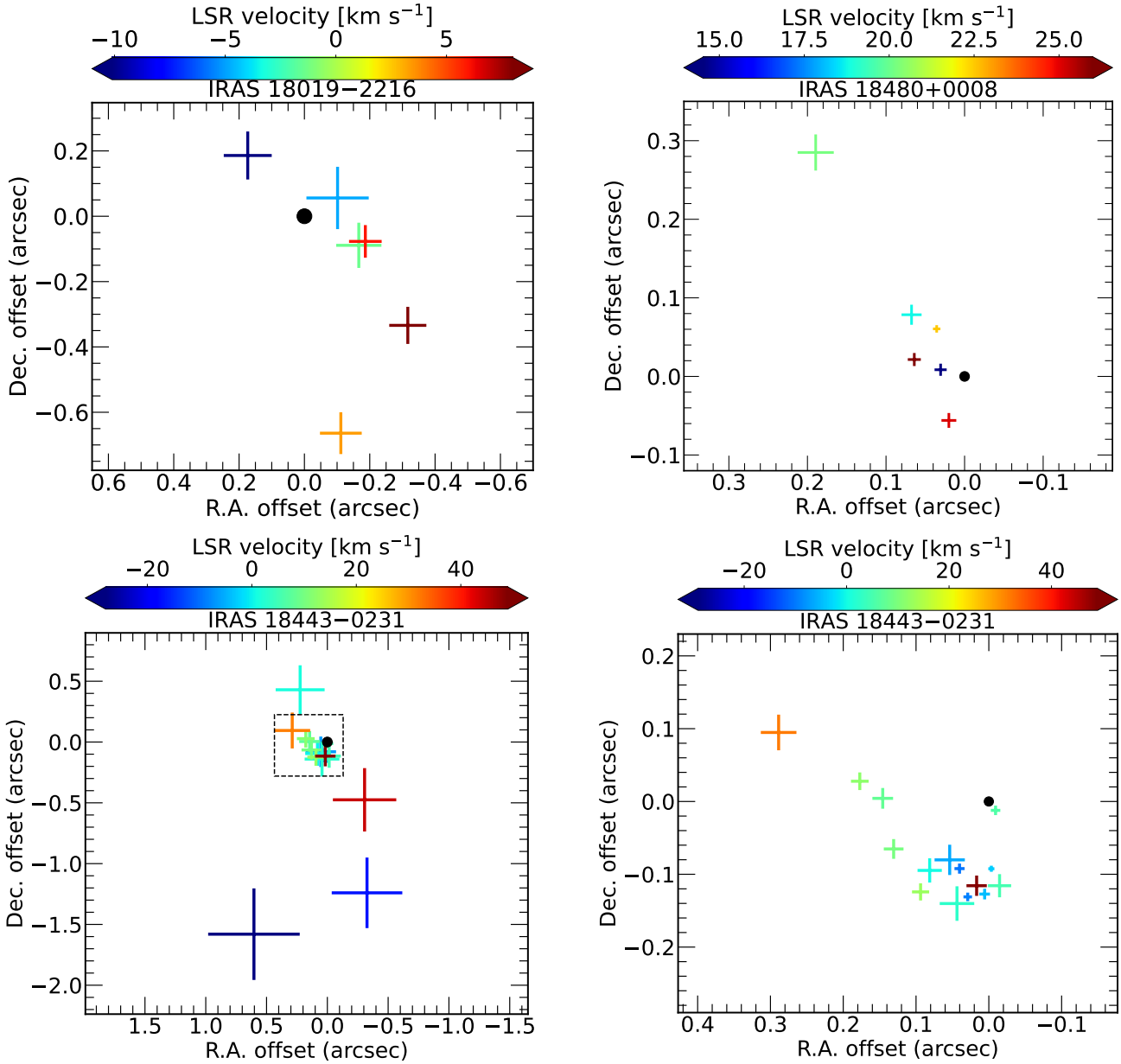

Fig. 2. Spatial distribution of the H_2O maser components (crosses) with respect to the position of the radio continuum emission peak (filled circle) at 22.22 GHz. The colorbar represent the LSR velocity of the masers and the symbols sizes are their positional uncertainties. The bottom right panel is a close-up of H_2O maser components in the central area of IRAS 18443−0231 (marked by a black dashed rectangle in the left panel), close to the continuum emission peak.

emission, such as YSOs or galaxies and therefore, could contaminate our group of candidates. For instance, the SED of YSOs usually peaks at wavelengths around 1 µm or longer than 70 µm (e.g. Robitaille et al. 2007). In the particular case of low-mass YSOs, radio continuum emission from shock-ionized jets is more prominent in the earlier stages (class 0 and class I sources), when the SED peaks at long wavelengths (>100 µm; Dunham et al. 2008, 2013). In the case of high-mass YSOs, the peak of the SED for H II regions (including ultracompact ones) usually lies at wavelengths longer than 70 µm (Wood & Churchwell 1989; Anderson et al. 2012).

In galaxies with active galactic nuclei, the peak of the SED seems to be at wavelengths shorter than 1 µm or longer than 100 µm (e.g. Dale et al. 2005; Popescu et al. 2011; Brown et al. 2014; Lyu & Rieke 2022). Thus, the differences between the SEDs in Fig. 3 and those of typical YSOs and galaxies indicate that our targets are more likely to be evolved objects. Moreover, among these, symbiotic stars (SySts) can also present maser emission (e.g., Cho & Kim 2010), although OH ones are extremely rare (e.g., Norris et al. 1984; Seaquist et al. 1995). The SED peak of SySts usually lies at $\lambda \leq 10$ µm (Akras et al. 2019). This only happens in two of the objects in Fig. 3, which will be discussed below. Therefore, the SED of most of the newly identified objects in this paper seems more consistent with post-AGB stars and PNe hosting maser emission.

5.2. Infrared morphologies

We inspected the available mid- and near-infrared images of the new IC sources reported in this work. All seem to be

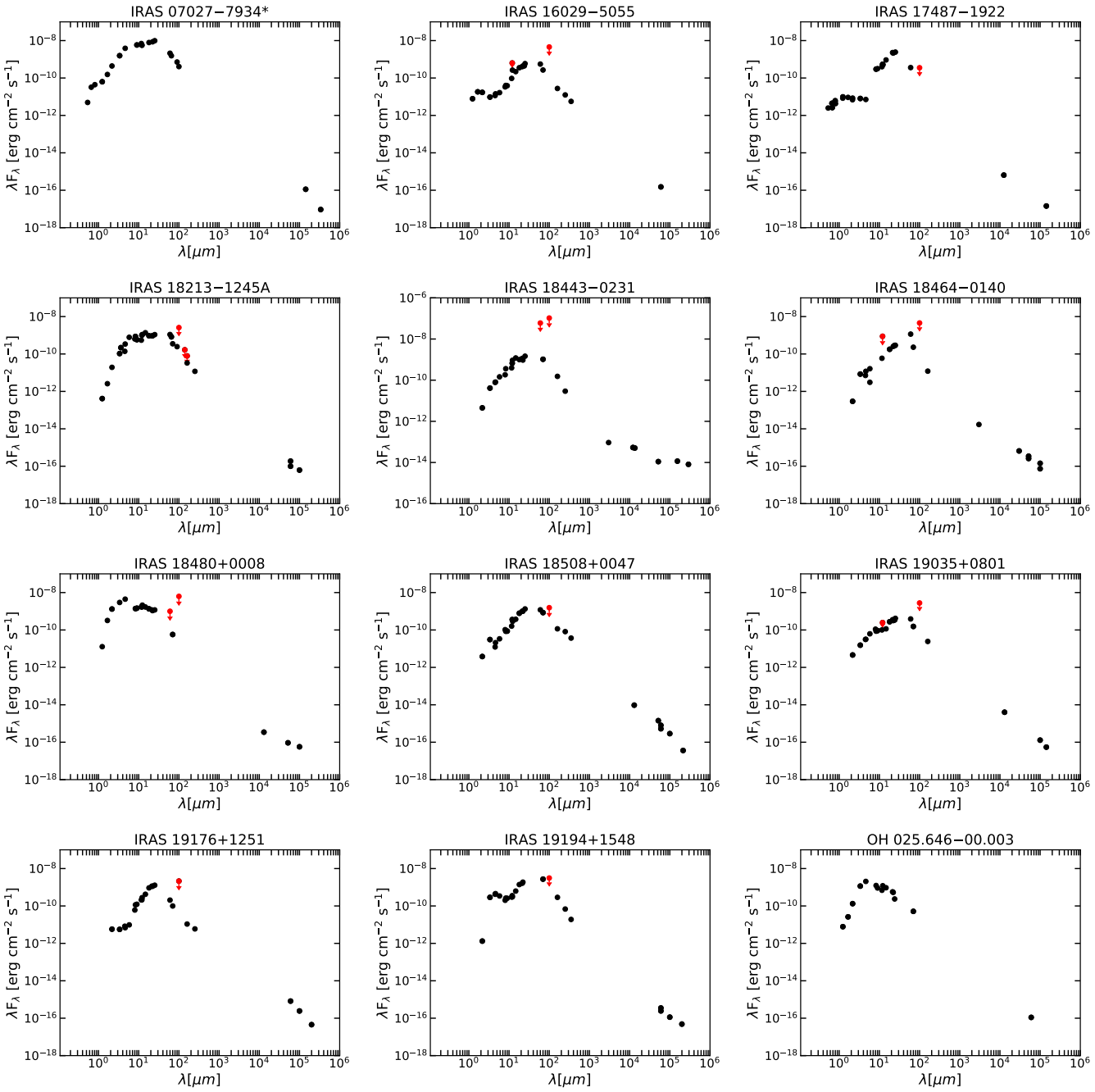

Fig. 3. SED of the new maser-emitting PN (indicated with an asterisk next to its name) and candidates (rest of the panels). The circles are the photometric values found for each of the new identified sources. The size of the circles is larger than the errors. Red color stands for upper limits.

compact sources in the mid-infrared, with the exception of IRAS 19194+1548, which is compact but marginally resolved. Furthermore, this source (Appendix C.2.6) shows a point-symmetric morphology in near-infrared images that is typical of evolved stars, rather than YSOs. The compact and isolated morphology of the sources classified as IC in this paper supports their identification as evolved stars rather than YSOs, which are usually surrounded by diffuse and extended structures from their parental clouds.

5.3. Mid-infrared colors

To further elucidate if the emission properties of the identified sources are more compatible with circumstellar envelopes of evolved stars, Fig. 4 shows an *MSX* color-color diagram of all known maser-emitting PNe and candidates (collecting the sources presented in this paper, and those previously reported in the literature). This color-color diagram, where each color is defined as $[a] - [b]$=2.5 $log(S_a/S_b)$, was presented by Sevenster (2002) to help identify post-AGB stars among evolved stars with OH maser emission, and later used by Uscanga et al. (2012) and Cala et al. (2022) in the characterization of maser-emitting PNe. We note that this diagram does not provide a clear-cut diagnosis of the nature of each source, but it shows quadrants where it is more likely to find sources of a particular type. The confirmed and candidate maser-emitting PNe cluster mainly in the quadrant of late post-AGB stars, as expected if they are all bona fide PNe. However, some interesting cases are identified in this paper,

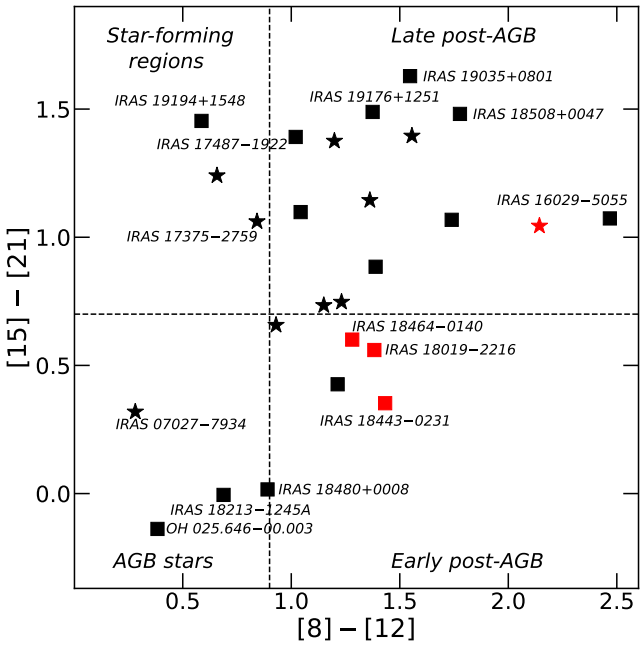

Fig. 4. *MSX* color-color diagram, as defined by Sevenster (2002), including all known and new maser-emitting PNe and candidates, and adopted from Cala et al. (2022). The vertical and horizontal dashed lines separate the diagram into four quadrants, where different types of sources tend to cluster. The filled star and square symbols without source names represent the previously reported maser-emitting PNe and candidates, respectively. These same symbols with source names are the new maser-emitting PNe and candidates, respectively. IRAS 16029−5055, IRAS 17375−2759 and IRAS 19176+1251 are included as PNe (see Section 5.4). Symbols with red color represent sources with WF characteristics.

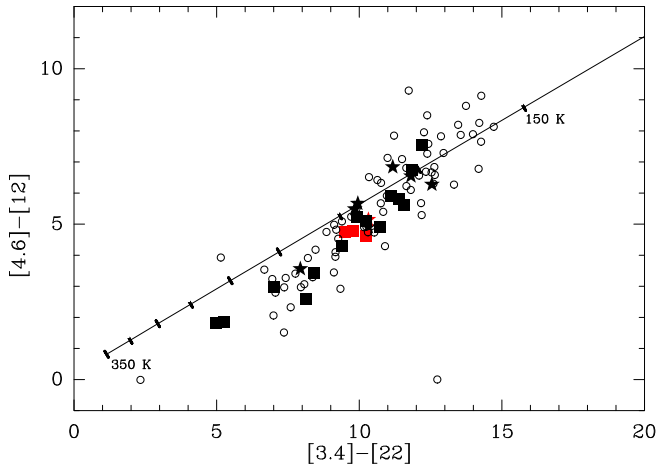

Fig. 5. *WISE* color–color diagram, similar to the one presented in Gómez et al. (2017), including all known and new maser-emitting PNe and candidates, and adopted from Cala et al. (2022). The stars and squares represent the confirmed maser-emitting PNe and candidates, respectively, as presented in Fig. 4. The red color stands for WF nature of the source. The open circles represent obscured post-AGB candidates (Ramos-Larios et al. 2009, 2012). The solid line represents the loci of the colors for blackbody brightness distributions. The tick marks in the blackbody line go from 150 to 350 K at increment steps of 25 K.

clearly located in the quadrant of AGB stars (the confirmed PN IRAS 07027-7934 and the candidate PNe IRAS 18123-1245A and OH 025.646-00.003), which deserve further attention. These objects may be rapidly evolving to the PN phase, while still retaining an envelope with AGB characteristics.

In Fig. 5 we show a *WISE* color-color diagram of all known and new maser-emitting PNe and candidates, adopted from Cala et al. (2022). The diagram was presented in Gómez et al. (2017) for a comparison between the colors of WFs and the optically obscured post-AGB stars. Cala et al. (2022) suggested that the colors 10.5≤[3.4]−[22]≤13.5, and 4.0≤[4.6]–[12]≤7.0 could identify new nascent PNe and candidates. Adding to this diagram the new confirmed and candidate maser-emitting PN found in this paper, we can see that these objects tend to cluster in the area delimited by the colors mentioned above. However, these limits are not strict, since some sources lie clearly outside of them. In particular, there are two candidates with [3.4]–[22]≃5 (IRAS 18480+0008 and OH 25.646−00.003), which seem to correspond to objects within or close to the quadrant of AGB stars in Fig. 4, suggesting that they may be different from the rest of confirmed or candidate maser-emitting PNe.

5.4. Mid-infrared spectra and diagnostic diagram

We have searched for *Spitzer* spectra of objects observed with the Infrared Spectrograph (IRS; Houck et al. 2004) and enhanced data products in the *Spitzer* Heritage Archive. We found spectra, obtained with the Short-Low (SL) and Short-High (SH) modules covering the range 5.13–14.29 μm and 9.9–19.6 μm, respectively, for two of the new OHPN candidates identified in this work, IRAS 16029−5055 (Program ID: 50652; PI: D. Engels) and IRAS 19176+1251 (Program ID: 30258; PI: P. Garcia-Lario), which we show in Fig. 6. We also found *Spitzer* spectra from one previously reported OHPN, IRAS 17393−2727 (Program ID: 3633; PI: M. Bobrowsky) (Pottasch et al. 1987; García-Hernández et al. 2007), and one previously reported OHPN candidate, IRAS 17375−2759 (Program ID: 3235; PI: M. Waelkens) (Uscanga et al. 2012), which are also shown in those figures, for comparison purposes. In addition, we found two highly processed archive spectra (2–45 μm) in the Infrared Space Observatory (ISO) data center[1] of IRAS 17347−3139 and K 3-35, two previously reported OHPN and H_2OPN (Miranda et al. 2001; de Gregorio-Monsalvo et al. 2004; Tafoya et al. 2009), which were shown in Uscanga et al. (2012), and we analyze them below, also for comparison purposes.

The *Spitzer* spectra shown in Fig. 6 display narrow and wide emission features commonly associated with ionized gas and dust grains, respectively. Usual ionized gas tracers are the fine-structure spectral lines of [Ar II], [Ar III], [Ne II], [Ne III], [Ne V], and [S IV] at 6.98, 8.98, 12.81, 15.55, 14.32, and 10.51 μm, respectively, while the broad features at 6.3, 8.6, and 11.6 μm are commonly associated with emission from polycyclic aromatic hydrocarbons (PAHs). In addition, there is spectrally resolved emission of PAHs at 7.4 μm. The spectra of galaxies, H II regions, and YSOs with low and high masses usually display an absorption feature at 9.8 μm (e.g., Peeters et al. 2004; Simpson et al. 2012), which is absent in the spectra shown here. Moreover, the lines of the ionized gas in this wavelength range are characteristic of PNe, and not of post-AGB stars (see also Matsuura et al. 2014, for *Spitzer* spectra of post-AGB stars and PNe in the Milky Way and Large Magellanic Cloud), so IRAS 16029−5055, IRAS 17375−2759, and IRAS 19176+1251 are likely to be PNe.

[1] The spectra presented by Uscanga et al. (2012) are available at the ISO data center and the technical report is available at https://nida.esac.esa.int/hpdp/technical_reports/technote52.pdf

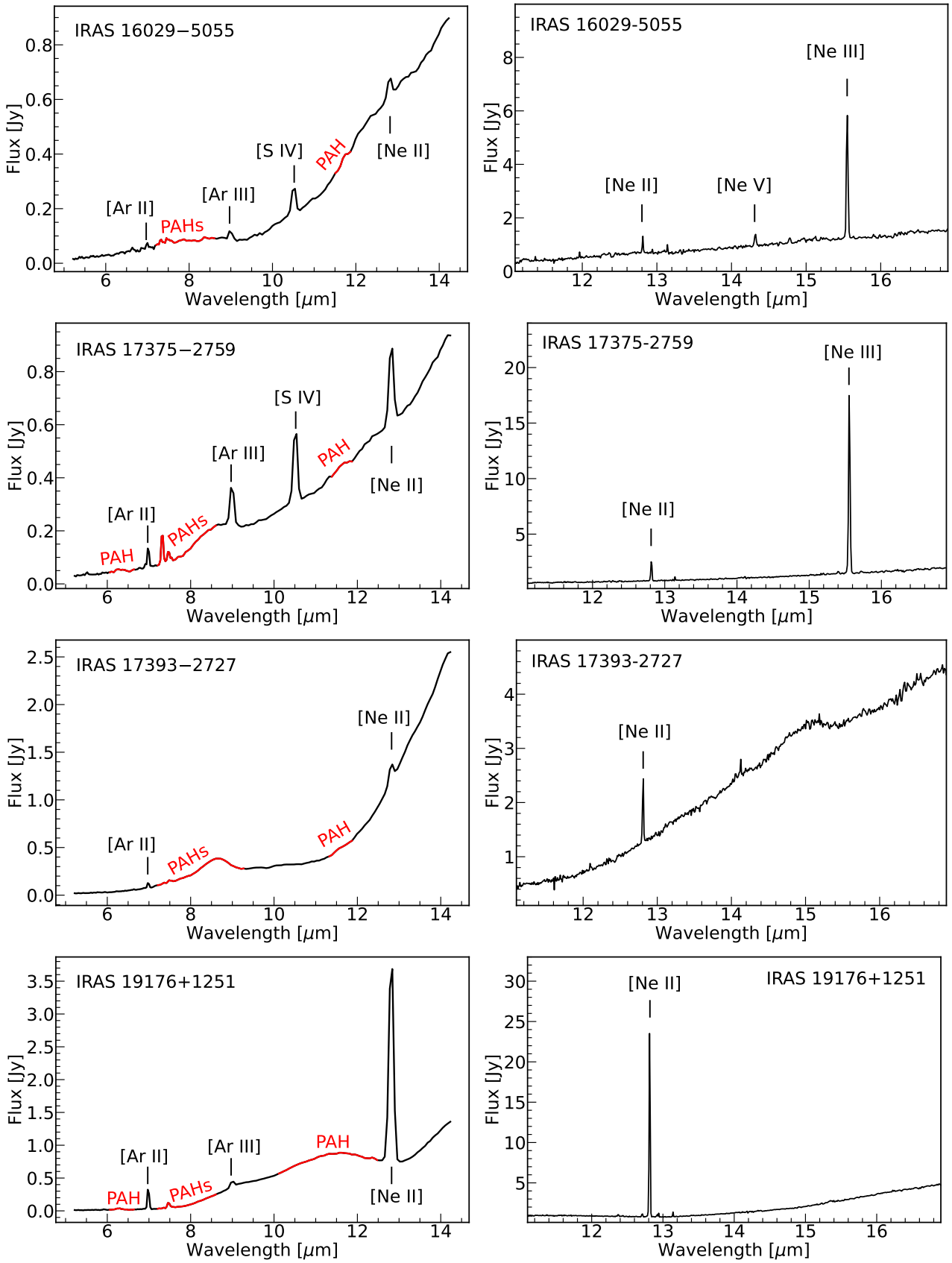

Fig. 6. Mid-infrared spectra of IRAS 16029−5055, IRAS 17375−2759, IRAS 17393−2727, and IRAS 19176+1251, as seen by the IRS SL (left) and SH (right) modules of *Spitzer*. Narrow and broad emission lines (red color) from ionized gas and dust grains, respectively, are present in their spectra. The narrow emission lines of [Ar II], [Ar III], [S IV], [Ne II], [Ne III], and [Ne V] are observed at around 6.98, 8.98, 10.51, 12.84 μm, 15.55, and 14.32 μm, respectively. The broad emission lines are usually attributed to emission from PAHs, which present a different chemistry (C-rich) from that of the O-rich maser-emitting regions.

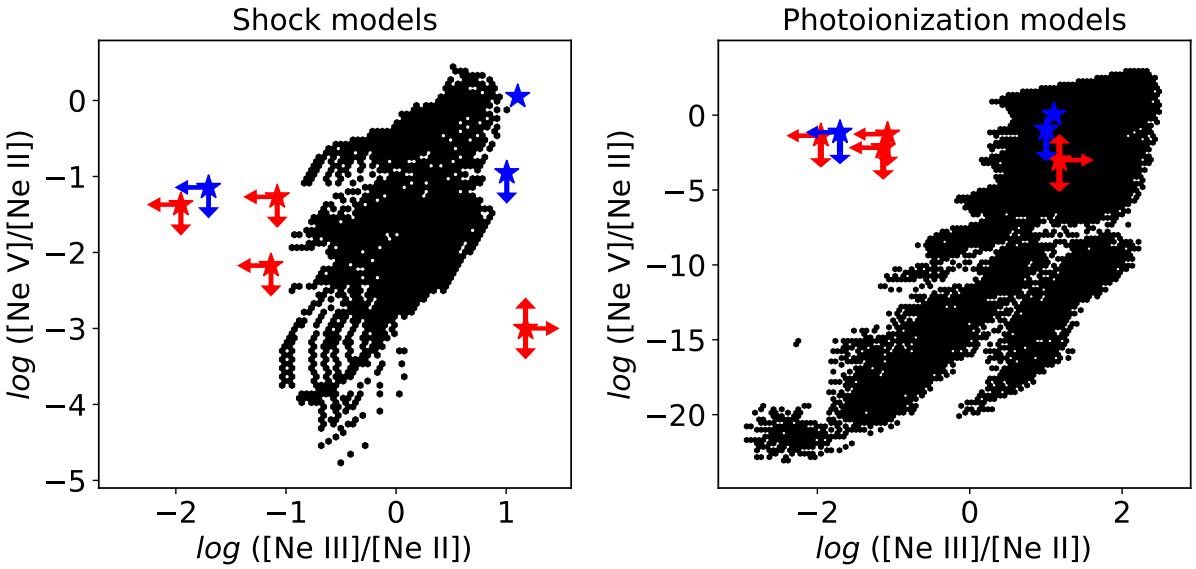

Fig. 7. Line ratio diagnostic diagram for the mid-infrared emission lines of [Ne II], [Ne III], and [Ne V] at 12.81, 15.55, and 14.32 μm, respectively. The left panel shows shock models, and the right panel shows photoionization models. The blue stars mark the new objects in which the presence of photoionized gas is favored by these diagrams (IRAS 16029−5055, IRAS 17375−2759, and IRAS 19176+1251). The red stars mark previously reported maser-emitting PNe (IRAS 17347−3139, IRAS 17393−2727, and K 3-35). The sizes of the symbols are larger than their errors. The arrows indicate values of line ratios that are either upper or lower limits, derived from the upper limits for the lines not detected in each case (see Fig. 6). In one case (K 3-35, red star with three arrows) the value *log* ([Ne V]/[Ne II]) is undetermined, and it could be located anywhere in the vertical direction. See Appendix D for more details on the grid parameters.

In order to better determine if these spectral lines tracing ionized gas in the mid-infrared actually identify these objects as PNe, we used the Mexican Million Models Database (3MdB; Morisset et al. 2015; Alarie & Morisset 2019), which allowed us to analyze whether the line intensities are consistent with shocks or photoionization. We have used the shock models of Sutherland & Dopita (2017) and the photoionization models of Ferland et al. (2017) stored in the 3MdB to create line-ratio diagnostic diagrams. We did not search for exact models to match the observed line ratios. Instead, we used the maximum number of models to define the entire region within these diagrams that is compatible to either origin of ionization. More details on the grid parameters are provided in the Appendix D. The final diagnostic diagram is shown in Fig. 7, displaying line ratios compatible with shock ionization and photoionization, which we compared with our data.

In this comparison, we have not corrected the spectra by extinction. This extinction is relatively low in the mid-infrared, and we have used ratios of lines that are close in wavelength ([Ne II], [Ne III] and [Ne V] seen at 12.81, 15.55, and 14.32 μm, respectively) so their line intensity ratios are practically insensitive to extinction (e.g., Genzel et al. 1998; Martín-Hernández et al. 2002; Pereira-Santaella et al. 2010; Weaver et al. 2010). In addition, each spectrum has been continuum-subtracted using a polynomial curve fitting, and then each emission line was measured with an individual Gaussian fitting using Astropy (Astropy Collaboration 2013, 2018, 2022).

Although we can reasonably expect that the origin of ionization in nascent PNe is a combination of both shocks and photoionization, the location of the sources in the line-ratio diagnostic diagrams that separate either process is revealing. The intensity ratios fall outside the region covered by the shock ionization models in all cases, specially in the [Ne III]/[Ne II] ratio, whereas they can be consistent with the photoionization models. The incompatibility with shocks alone indicates that these fine-structure spectral lines must have a significant photoionization contribution. Therefore, these models favor the presence of photoionized gas in IRAS 16029−5055, IRAS 17375−2759, and IRAS 19176+1259. For comparison, previously reported maser-emitting PNe IRAS 17347−3139, IRAS 17393−2727, and K 3-35 also fall outside the region of shock models in Fig. 7 (left).

5.5. Spectral indices and variability of the radio continuum emission

The dependence of the flux density (S_ν) of the radio continuum emission with frequency (ν) can give useful hints on the emission processes and therefore on the nature of the sources. Spectral indices (α, with $S_\nu \propto \nu^\alpha$) of thermal (free-free) emission of the photoionized gas in PNe must be in the range from +2 at low frequencies (optically thick regime) and −0.1 at high frequencies (optically thin regime). The observed radio spectra usually show two different ranges (e.g., Taylor et al. 1987; Aaquist & Kwok 1991; Gruenwald & Aleman 2007). At low frequencies, α ranges from $\simeq +0.6$ to +2, indicating (partially) optically thick emission, while at high frequencies the slope flattens to values $\alpha \simeq -0.1$. The turn-over frequency separating both regimes can be used to estimate the emission measure (EM) of the nebulae that, in its turn, is thought to be related with age, with younger PN having higher EM (Kwok et al. 1981). Thus, the turn-over frequencies would tend to decrease with time. In the particular case of a nascent PN, while the ionization front advances at supersonic velocities (R-type ionization front, Kahn 1954; Franco et al. 1990), the plasma still briefly maintains the density distribution of the circumstellar envelope created by mass-loss in the AGB phase, with a radial dependence of the electron density to be $n_e \propto r^{-2}$. In this case, the radio spectral index must be around +0.6 (partially optically thick) in most of the centimeter domain (see e.g., Olnon 1975; Panagia & Felli 1975). Spectral indices on this order, and high turn-over frequencies (>20 GHz)

are indeed observed in nascent PNe (e.g., Gómez et al. 2005; Cala et al. 2022). However, we note that the same spectral index is also expected in the case of shock-ionized winds, including biconical jets (Reynolds 1986), which could be present before the PN phase. In this case, considerations of the required mass-loss rate to produce the observed flux densities can help us to discern if the emission is compatible with shock ionization or photoionization (see Tafoya et al. 2009; Uscanga et al. 2014). One of such cases is IRAS 17347−3139, which was reported before as PN because the required mass-loss rates are incompatible with shock ionization alone (Tafoya et al. 2009), and in this work (Sect. 5.4) we spectroscopically confirmed the presence of photoionized gas in this object and, therefore, corroborated that it is a PN.

Together with the radio continuum emission in our data, we collected publicly available measurements of flux densities in our targets at different frequencies. Recent observational efforts have aimed at updating and creating new all-sky radio continuum surveys such as, for instance, the VLA Sky Survey (VLASS; Gordon et al. 2021), Co-Ordinated Radio 'N' Infrared Survey for High-mass star formation (CORNISH; Irabor et al. 2018, 2023), GLObal view on Star formation in the Milky Way (GLOSTAR; Medina et al. 2019; Dzib et al. 2023), Rapid Australian SKA Pathfinder (RASKAP; Hale et al. 2021), or The HI/OH/Recombination line survey of the inner Milky Way (THOR; Wang et al. 2018).

Maser-emitting PNe and candidates show increasing flux densities in timescales of years and decades (Gómez et al. 2005; Tafoya et al. 2009; Cala et al. 2022), with the exception of IRAS 15103−5754, which shows a decrease non-thermal radio continuum emission in timescales of a few months (Suárez et al. 2015). Hence, simultaneous observations across a large part of the centimeter domain are crucial to obtain a precise determination of the radio spectral indices. Using data at different frequencies taken at different epochs can result in unrealistic slopes in the radio spectrum, so special care should be taken in these cases. Obtaining spectral indices from different catalogs or observational projects can provide a useful first approximation, but a definite confirmation of the actual radio spectrum can only be obtained with (quasi-)simultaneous observations. In our case, while flux densities reported in the surveys mentioned above can be used to obtain preliminary radio spectra of the new identified maser-emitting sources, we can obtain even more solid confirmation of the spectral indices by focusing only on the measured flux density values at different frequencies in our own observations for several targets, which were taken within less than eight days for each individual source (Table A.1).

Fig. 8 shows the flux densities and determined spectral indices of the new maser-emitting PNe and candidates, using the data from our observations (black symbols) and from the surveys mentioned above (red and blue symbols). The black and blue symbols were used in the fits to estimate spectral indices. In the case of the red points, most of them were obtained from an earlier epoch than the blue ones and/or our data. In particular, the red point of IRAS 17487−1922 was reported by VLASS from observations performed on 30/06/2019, which significantly deviates from the observed tendency from the data points of our own VLA observations; the one of IRAS 17494−2645 was discussed by Cala et al. (2022); the one in IRAS 18213−1245A was reported by White et al. (2005); in IRAS 18464−0140 the red point at 5 GHz was reported by White et al. (2005), and that at 10 GHz is from 08/03/2022 (see Section 3.2), which is the only one that is from a more recent epoch; in IRAS 18508+0047, the red point at 1.4 GHz was reported by Becker et al. (1994), while those at 5 GHz were reported by White et al. (2005) and Urquhart et al. (2009); the red point in IRAS 19194+1548 was reported by Urquhart et al. (2009). These red points were not used in the spectral index fit, since they consistently show lower flux densities and where obtained at a significantly different time than other data, but are useful to illustrate the variability of the objects. The new OHPN candidates IRAS 16029−5055 and OH 025.646−00.003 are not presented in this figure, since we found only one flux density value available in the literature with no other data in the ATCA and VLA archives, and thus we cannot obtain the spectral index values of these sources.

The radio spectrum of most of the sources identified here seems compatible with free-free emission and, therefore, these sources could be PNe. These indices would further suggest that they are not background galaxies or pulsars, which tend to show negative spectral indices, due to the non-thermal nature of their emission (e.g. Maron et al. 2000). The most noticeable exception is IRAS 18443−0231, for which the obtained α=−0.42±0.05 from our VLA observations between 1–24 GHz is consistent with non-thermal radio continuum emission. This result is robust, since it was obtained from our observations and taken close in time. This source is described in detail in Appendix C.2.3, providing strong arguments that it is an evolved star, despite its non-thermal radio continuum spectrum.

For some sources, there are indications of a spectral index change along the spectrum, although we cannot always confirm this due to the lack of quasi-simultaneous observations at different frequencies. The study of the turnover frequencies is interesting, since they may reveal some additional information. For example, the turnover between $\alpha\simeq$+0.6 and −0.1 in a nascent PN could indicate that the electron density in the innermost regions falls well below the $n_e \propto r^{-2}$ law. This could happen if there is an inner, non-ionized hole close to the central star (Anglada et al. 2018). Such a central hole is expected, since the PN is the result of ionizing a circumstellar envelope ejected in previous evolutionary phases. The size of such a hole will increase as the PN evolves, causing this turnover frequency to decrease with time. A possible example of such a turnover to optically thin emission ($\alpha\simeq$−0.1) at high frequencies is IRAS 18019−2216. Assuming a turnover frequency of 8 GHz, the radius of this hole would be of $\simeq$12 au × d for a spherical ionized region surrounding that hole, where d is the distance in kpc from the object (see Eq. (10) of Anglada et al. 2018), a small size that would be consistent with a young PN. On the other hand, a turnover between the optically thick regime ($\alpha\simeq$+2) and the standard $\alpha\simeq$+0.6 expected in nascent PNe may trace the existence of a sharp outer boundary in the ionized nebula. As the ionization front advances in a nascent PN, one could also expect this turnover frequency to decrease over time. Possible sources with this turnover frequency from $\alpha\simeq$+2 to +0.6 are IRAS 18508+0047 and IRAS 19035+0801. However, only in the latter case can our own data, obtained close in time, give more solid support to this change of spectral index.

As mentioned above, the points marked in red in Fig. 8 are data from the literature that were not used in the fit of spectral indices because they were obtained at a significantly different epoch than the blue or black ones. In several cases, they clearly depart from the fit. This shows a clear trend of flux density increase with time. This has been found in other confirmed and candidate maser-emitting PNe (e.g. Gómez et al. 2005; Cala et al. 2022), and has been interpreted as tracking the growth of pristine ionizing regions at the beginning of the PN phase.

Therefore, the combined evidence provided by the spectral indices and variability of the radio continuum emission

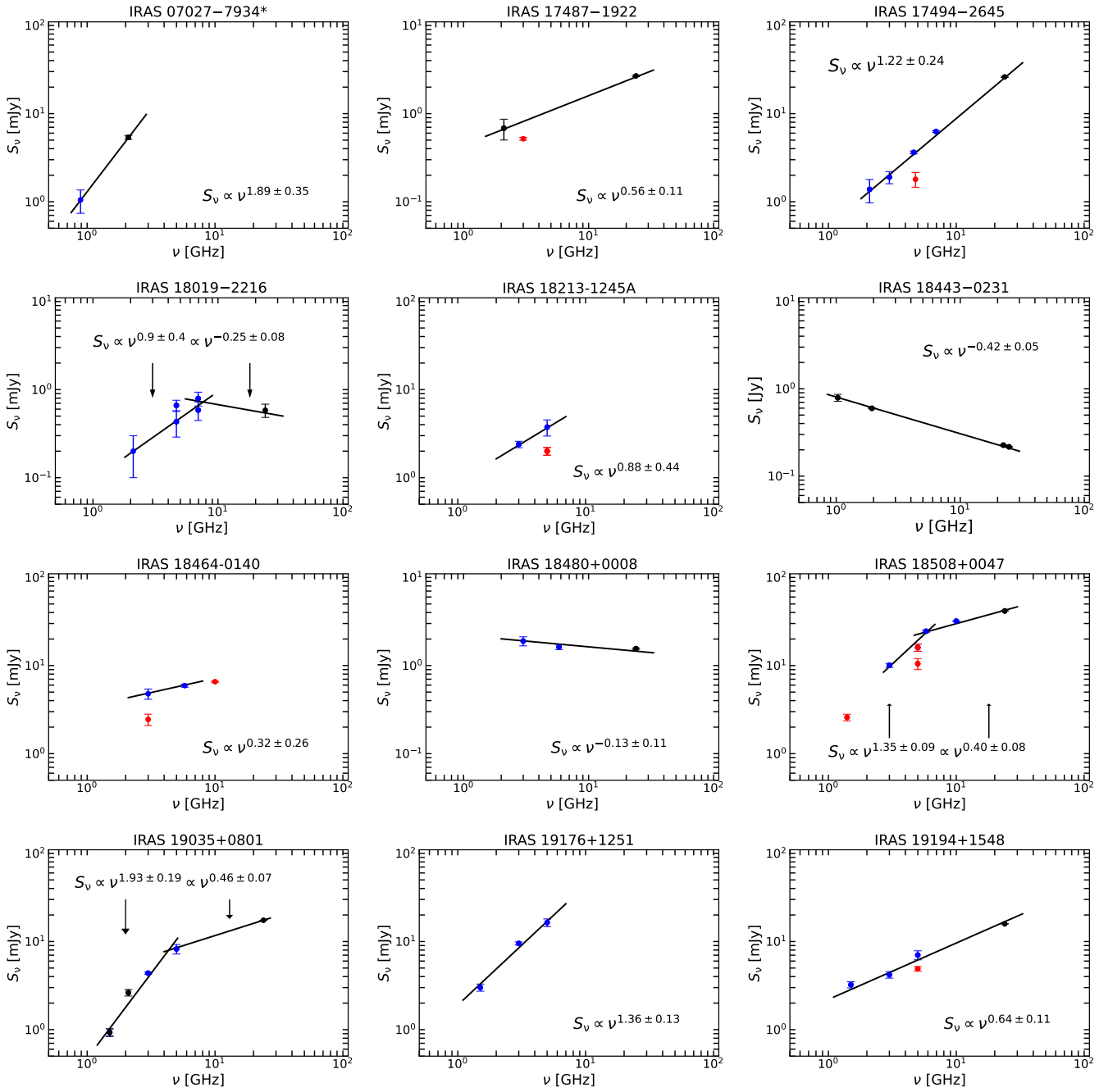

Fig. 8. Radio continuum emission of the new maser-emitting PN (indicated with an asterisk next to its name) and candidates (rest of the panels), including the new flux density values at 24.5 GHz from our VLA observations in the previously reported OHPN candidates IRAS 17494−2645 and IRAS 18019−2216 (Cala et al. 2022). The source names and obtained spectral indices (α) are indicated in each panel. Black circles are data from our ATCA/VLA observations. Blue circles are data from the literature which, together with the black circles, were employed to fit the spectral indices. Red circles correspond to values from epochs earlier than the blue and black ones, except for IRAS 18464−0140, where the point at 10 GHz is from a more recent epoch. Thus, these red points were not used in the spectral index fits, since they were obtained at a significantly different epoch. See the text for more details.

provides further support that the sources identified in this work are compatible with being nascent PNe.

6. Discussion

As a summary after our results in this paper, in Table 2 we report the total number of maser-emitting PNe and candidates identified in this work, together with those previously reported in other works. We have increased the number of confirmed maser-emitting PNe known to nine, while the number of candidates has increased to 16. In addition, we have increased the number of WFs to 18 (Table E.1), including the first two 'low-velocity' WFs radio continuum emitters.

This increase in candidate maser-emitting PNe is an important step forward, although eventually confirming their nature as bona-fide PNe would be crucial to better understand the nature and properties of this category of sources.

Table 2. List of all known maser-emitting PNe and candidates.

Name	Alt. name	Galactic coordinates	Maser emission[a]			Status[c]	References[b]			
			SiO	H_2O	OH		SiO	H_2O	OH	Nature
IRAS 07027−7934	Vo 1	291.375−26.294	–	No	Yes	IP	–	1	TW	2, 3
IRAS 15103−5754	GLMP 405	320.907−00.293	No	Yes	–	IP	4	5	–	5, 6
IRAS 16029−5055	SCHD 68	331.158+00.781	–	–	Yes	IC	–	–	7	TW
IRAS 16333−4807		336.644−00.696	No	Yes	Yes	IP	4	8	9	8, 9
IRAS 16372−4808	SCHD 117	337.064−01.173	No	No	Yes	IC	4	10	11	12
IRAS 17150−3754	PBZ 1	349.351−00.211	–	No	Yes	IC	–	–	13	13
IRAS 17347−3139	RPZM 28	356.801−00.055	No	Yes	Yes	IP	4	14	15	14, 16, 15, TW
IRAS 17371−2747	JaSt 23	000.340+01.574	No	–	Yes	IP	4	–	17	18, 19
IRAS 17375−2759	PBOZ 26	000.208+01.412	–	–	Yes	IC	–	–	20	19, TW
IRAS 17393−2727	OH 0.9+1.3	000.892+01.341	No	–	Yes	IP	4	–	13	13, 21, TW
IRAS 17487−1922	OH 008.9+03.7	008.905+03.712	–	No	Yes	IC	–	TW	TW	TW
IRAS 17494−2645	SCHB 220	002.640−00.191	–	No	Yes	IC	–	TW	22	12, TW
IRAS 18019−2216	SCHB 281	007.958−00.393	–	Yes	Yes	IC	–	TW	23	12, TW
IRAS 18061−2505	MaC 1-10	005.974−02.611	No	Yes	No	IP	4	24	24	24, 25
IRAS 18213−1245A		018.526+00.150	–	Yes	Yes	IC	–	26	27	TW
IRAS 18443−0231	RFS 505	030.234−00.138	–	Yes	No	IC	–	TW	TW	TW
IRAS 18464−0140	OH 31.21−0.18	031.213−00.180	–	Yes	Yes	IC	–	28	28	TW
IRAS 18480+0008		033.023+00.279	–	Yes	Yes	IC	–	TW	27	TW
IRAS 18508+0047	GPSR5 33.906–0.044	033.906−00.043	–	No	Yes	IC	–	TW	27	TW
IRAS 19035+0801	PM 1-279	041.787+00.488	–	No	Yes	IC	–	TW	TW	TW
IRAS 19176+1251	GLMP 898	047.688−00.302	–	No	Yes	IC	–	29	27	TW
IRAS 19194+1548		050.480+00.705	–	No	Yes	IC	–	TW	27	30, TW
IRAS 19219+0947	Vy 2-2	045.498−02.703	No	No	Yes	IP	4	31	32	33, 32
IRAS 19255+2123	K 3-35	056.096+02.094	No	Yes	Yes	IP	4	34	34	35, 34, TW
OH 25.646−0.003		025.646−00.003	–	No	Yes	IC	–	27	TW	TW
OH 341.681+00.264		341.681+00.263	No	–	Yes	IC	4	–	11	12

Notes. [a] '–': no interferometric observations available. [b] Reference for the interferometric maser emission detected. In the nature column, we provide references that have contributed to classifying the source as a PN candidate or confirmed PN. TW: This work. [c] As defined in Table 1. 1. Suárez et al. (2009). 2. Menzies & Wolstencroft (1990). 3. Surendiranath (2002). 4. Cala et al. (2024a). 5. Gómez et al. (2015b). 6. Suárez et al. (2015). 7. Sevenster et al. (1997). 8. Uscanga et al. (2014). 9. Qiao et al. (2016a). 10. Deacon et al. (2007). 11. Qiao et al. (2016b). 12. Cala et al. (2022). 13. Pottasch et al. (1987). 14. de Gregorio-Monsalvo et al. (2004). 15. Tafoya et al. (2009). 16. Gómez et al. (2005). 17. Sevenster (2002). 18. Jacoby & Van de Steene (2004). 19. Uscanga et al. (2012). 20. Zijlstra et al. (1989). 21. García-Hernández et al. (2007). 22. Qiao et al. (2018). 23. Qiao et al. (2020). 24. Gómez et al. (2008). 25. Miranda et al. (2021). 26. Walsh et al. (2014). 27. Beuther et al. (2019). 28. Forster & Caswell (1999). 29. Gómez et al. (2015a). 30. Sabin et al. (2014). 31. Gómez et al. (1990). 32. Seaquist & Davis (1983). 33. Vyssotsky et al. (1945). 34. Miranda et al. (2001). 35. Miranda et al. (2000). IC: interferometrically confirmed maser-emitting PN candidate. IP: interferometrically confirmed maser-emitting PN.

To confirm the identified PN candidates as bona fide maser-emitting PNe, it is first necessary to ascertain the presence of photoionized gas. Considering that these candidates are, in general, optically obscured objects, we suggest that this confirmation can be achieved by means of near- and mid-infrared spectroscopic observations, complemented with a comparison of the observed emission line ratios with diagnostic diagrams that represent photoionization and shock ionization models. A first attempt has been made for some sources in Section 5.4. Using several diagnostic diagrams involving different line rations would strongly support whether or not photoionized gas is present in our objects. Furthermore, high-resolution imaging of the emission lines that are used to create diagnostic diagrams, such as those of [Ne II] and [Ne III] shown in Fig. 7, should be obtained in order to create spatially resolved maps of emission line ratios across the ionized circumstellar nebula, pinpointing the distribution of the photoionized gas from the PN. In addition, high-resolution imaging of radio and millimeter/submillimeter recombination lines can also reveal whether their kinematics is more consistent with an ionized wind, or with the expansion of a photoionized nebula.

Even if we could confirm as PNe a significant number of the identified candidates, their numbers may still be scarce to draw firm conclusions about important issues such as their evolutionary status, or whether they all evolve from stars with similar characteristics (e.g., initial masses, metallicity). It is then important to continue working on increasing the number of known members of this type of sources, for instance, confirming the nature of the identified candidates as PNe (by means of optical and infrared spectroscopy) or undergoing new sensitive mappings of masers in our Galaxy, such as the future Galactic Australian Square Kilometre Array Pathfinder (GASKAP)-OH project (Dawson et al. 2024).

In addition to the scarcity of known maser-emitting PNe, observational biases are also a potential problem to understand properties such as the nature, timescales, or prevalence of maser emission in PNe. Many searches for masers in evolved stars have selected their target samples based on particular infrared

properties (e.g. Davis et al. 1993; te Lintel Hekkert & Chapman 1996), which may leave out many PNe. These biases are being mitigated by the increasing number of published maser surveys, which performed a complete mapping of wide regions throughout the Galactic center and plane (e.g. Walsh et al. 2014; Beuther et al. 2019; Qiao et al. 2016b, 2018, 2020). Keeping in mind these caveats, the current list of sources can start to provide some interesting patterns, although they will have to be taken with care.

The infrared properties of these maser-emitting sources, as shown in the *MSX* (Fig. 4) and *WISE* (Fig. 5) color–color diagrams, seem very diverse, as they populate all regions of those diagrams. In principle, this suggests that they do not constitute a homogeneous group and that different types of PNe can give rise to maser emission. However, there are hints of a higher density of sources in certain regions of the color–color diagrams, such as the top right quadrant in Fig. 4 and 9≤[3.4]−[22]≤13 in Fig. 5, probably indicating that PNe with particular properties have a higher tendency to pump masers.

In line with the suggestion of Cala et al. (2024b), we found, apart from the known case of IRAS 17347−3139, one more OHPN (IRAS 17393−2727) and three more OHPN candidates (IRAS 16029−5055, IRAS 17375−2759, and IRAS 19176+1251) that could have mixed chemistry, with O-rich outer envelopes (where OH and H_2O masers are emitted), but with C-rich inner nebulae and/or central stars (see Sect. 5.4). Thus, they could potentially be similar to IRAS 07027−7934 and IRAS 18061−2505, which harbor C-rich central stars of the type [WC] (see Zijlstra et al. 1989; Miranda et al. 2021, and Sect. C.1). In general, PNe harboring [WC] have been found surrounded by both O- and C-rich dust (e.g., de Marco & Soker 2002), but only in these PNe does the presence of masers link the [WC] with an O-rich star progenitor in the AGB phase. Hence, these PNe are potentially key in characterizing the formation mechanisms of [WC], which may involve a recent thermal pulse and/or a common envelope (see Ivanova et al. 2013; Zou et al. 2020, and references therein). A common envelope has previously been suggested in the formation and evolution of other maser-emitting PNe (Gómez et al. 2018a; Miranda et al. 2021). In any case, the formation mechanisms of [WC] are still not completely understood (e.g. de Marco & Soker 2002; García-Rojas et al. 2018; Hajduk et al. 2020).

In this paper we have also identified two objects (IRAS 18019−2216 and IRAS 18464−0140) which could be classified as 'low-velocity' WFs because they show bipolar H_2O maser distributions, a velocity coverage of the H_2O masers larger or in a range different from that of the OH masers, but a H_2O maser velocity coverage of only tens of km s^{-1} (Yung et al. 2013; Fan et al. 2024), in contrast to the usual velocity spreads of hundreds of km s^{-1} of classical WFs (Table E.1). Yung et al. (2013) found that WFs with low velocity masers showed infrared colors suggesting that they are in the late AGB or early post-AGB phases. If this is correct, IRAS 18019−2216 and IRAS 18464−0140 would probably not be PNe, and their radio continuum emission would arise from shock-ionized gas.

7. Conclusions

We have undergone an extensive search for new maser-emitting PNe. Our main conclusions are as follows.

- We have increased the number of confirmed maser-emitting PNe known to nine and increased the number of candidates to 16. Furthermore, we have increased the number of known WFs to 18, and reported the first two 'low-velocity' WFs emitters of radio continuum;
- The wide distribution of maser-emitting PNe in the *MSX* and *WISE* color-color diagrams suggests that they do not constitute a homogeneous group and that PNe of different properties may host maser emission during its evolution. However, there is some evidence that PNe with particular infrared properties may have a higher tendency to pump maser emission;
- In addition to the OHPN IRAS 07027−7934 and the H_2OPN IRAS 18061−2505, which had already been shown to host a [WC] central star with an O-rich envelope, we report the presence of PAH emission in one more OHPN (IRAS 17393−2727) and three more OHPN candidates (IRAS 16029−5055, IRAS 17375−2759, and IRAS 19176+1251), suggesting that they may also show mixed chemistry, with C-rich central star or inner circumstellar regions. Together with the OHPN and H_2OPN IRAS 17347−3139, previously reported with PAHs, they could represent an emergent group of PNe that underwent a recent thermal pulse and/or common envelope evolution;
- The new interferometrically confirmed WF IRAS 18443−0231 shows strong and variable non-thermal radio continuum emission, as in magnetized outflows, and near infrared spectroscopy indicates ionized emission compatible with both shocks and photoionization. More research is needed on this object to confirm it as a PN.

Acknowledgements. The Australia Telescope Compact Array is part of the Australia Telescope National Facility (grid.421683.a) which is funded by the Australian Government for operation as a National Facility managed by CSIRO. We acknowledge the Gomeroi people as the traditional owners of the Observatory site. The National Radio Astronomy Observatory is a facility of the National Science Foundation operated under cooperative agreement by Associated Universities, Inc. We used continuum images from the VLA Sky Survey, downloaded from the Canadian Initiative for Radio Astronomy Data Analysis (CIRADA), which is funded by a grant from the Canada Foundation for Innovation 2017 Innovation Fund (Project 35999), as well as by the Provinces of Ontario, British Columbia, Alberta, Manitoba and Quebec. This work has made use of the SIMBAD database, operated at the CDS, Strasbourg, France, and the NASA/IPAC Infrared Science Archive, which is operated by the Jet Propulsion Laboratory, California Institute of Technology, under contract with the National Aeronautics and Space Administration. It also makes use of data products from 2MASS (a joint project of the University of Massachusetts and the Infrared Processing and Analysis Center/California Institute of Technology, funded by NASA and the NSF), AKARI (a JAXA project with the participation of ESA), DENIS (partly funded by the SCIENCE and the HCM plans of the European Commission under grants CT920791 and CT940627), HERSCHEL (Herschel is an ESA space observatory with science instruments provided by European-led Principal Investigator consortia and with important participation from NASA), IRAS (was a joint project of the US, UK and the Netherlands), Pan-STARRS (have been made possible through contributions by the Institute for Astronomy, the University of Hawaii, the Pan-STARRS Project Office, the Max-Planck Society and its participating institutes), *Spitzer* Space Telescope (operated by the Jet Propulsion Laboratory, California Institute of Technology under a contract with NASA), MSX (funded by the Ballistic Missile Defense Organization with additional support from NASA Office of Space Science), UKIDSS (The project is defined in Lawrence et al. (2007) and uses the UKIRT Wide Field Camera (WFCAM; Casali et al. 2007) and a photometric system described in Hewett et al. (2006). The pipeline processing and science archive are described in Hambly et al. (2008)), USNO-B catalog (the construction and contents of the catalog can be found in Monet et al. 2003), VVV survey (is supported by the European Southern Observatory, by BASAL Center for Astrophysics and Associated Technologies PFB-06, by FONDAP Center for Astrophysics 15010003, by the Chilean Ministry for the Economy, Development, and Tourism's Programa Iniciativa Científica Milenio through grant P07-021-F, awarded to The Milky Way Millennium Nucleus), and WISE (a joint project of the University of California, Los Angeles, and the Jet Propulsion Laboratory/California Institute of Technology, funded by the NASA). We also used the VLASS QLimage cutout server at URL cutouts.cirada.ca, operated by the Canadian Initiative for Radio Astronomy Data Analysis (CIRADA). CIRADA

is funded by a grant from the Canada Foundation for Innovation 2017 Innovation Fund (Project 35999), as well as by the Provinces of Ontario, British Columbia, Alberta, Manitoba and Quebec, in collaboration with the National Research Council of Canada, the US National Radio Astronomy Observatory and Australia's Commonwealth Scientific and Industrial Research Organisation. This work made use of Astropy[2]: a community-developed core Python package and an ecosystem of tools and resources for astronomy (Astropy Collaboration 2013, 2018, 2022). RAC, JFG, LFM, GA are financially supported by grants PID2020-114461GB-I00, PID2023-146295NB-I00, and CEX2021-001131-S, funded by MCIN/AEI/10.13039/501100011033. RAC also acknowledges support by the predoctoral grant PRE2018-085518, funded by MCIN/AEI/ 10.13039/501100011033 and by ESF Investing in your Future. K.O. acknowledges the support of the Agencia Nacional de Investigación Científica y Desarrollo (ANID) through the FONDECYT Regular grant 1240301.

References

Aaquist, O. B., & Kwok, S. 1991, ApJ, 378, 599
Akras, S., Guzmán-Ramírez, L., Leal-Ferreira, M. L., et al. 2019, ApJS, 240, 21
Alarie, A., & Morisset, C. 2019, Rev. Mex. Ast., 55, 377
Allen, M. G., Grovez, B. A., Dopita, M. A., et al. 2008, ApJS, 178, 20
Anglada, G., Estalella, R., Pastor, J., et al. 1996, ApJ, 463, 205
Anglada, G., Rodríguez, L. F., & Carrasco-González, C. 2018, A&A Rev., 26, 3
Anderson, L. D., Bania, T. M., Balser, D. S., et al. 2011, ApJS, 194, 32
Anderson, L. D., Zavagno, A., Barlow, M. J., et al. 2012, A&A, 537, A1
Arkhipova, V. P., Burlak, M. A., Esipov, V. F., et al. 2017, Astron. Lett., 43, 12, pp. 911
Astropy Collaboration (Robitaille, T. P., et al.) 2013, A&A, 558, A33
Astropy Collaboration (Price-Whelan, A. M., et al.) 2018, AJ, 156, 123
Astropy Collaboration (Price-Whelan, A. M., et al.) 2022, AJ, 935, 167
Avinson, A., Quinn, L. J., Fuller, G. A., et al. 2016, MNRAS, 461, 136
Becker, R. H., White, R. L., Helfand, D. J., et al. 1994, ApJS, 91, 347
Beuther, H., Walsh, A., Wang, Y., et al. 2019, A&A, 628, A90
Benson, P. J., & Little-Marenin, I. R., 1996, ApJS, 106, 579
Benson, P. J., Little-Marenin, I. R., Woods, T. C., et al. 1990, ApJS, 74, 911
Blöcker, T. 1995b, A&A, 299, 755
Boboltz, D. A., & Marvel, K. B. 2005, ApJ, 627, L45
Brown, M. J. I., Moustakas, J., Smidth, J. D. T., et al. 2014, ApJS, 212, 18
Cala, R. A., Gómez, J. F., Miranda, L. F., et al. 2022, MNRAS, 516, 2235
Cala, R. A., Gómez, J. F., Miranda, L. F., et al. 2024a, A&A, 692, A24
Cala, R. A., Gómez, J. F., Miranda, L. F., et al. 2024b, in Cosmic Masers: Proper Motion toward the Next-Generation Large Projects, IAU Symp 380, eds. T. Hirota, H. Imai, K. Menten, Y. Pihlström (Cambridge: Cambridge University Press), 343
Cala, R. A., Miranda, L. F., Gómez, J. F., et al. 2024c, A&A, 691, A321
CASA Team (Bean, B., et al.) 2022, PASP, 134, 114501
Casali, M., Adamson, A., Alves de Oliveira, C., et al. 2007, A&A, 467, 777
Cerrigone, L., Trigilio, C., Umana, G., et al. 2011, MNRAS, 412, 1137
Cerrigone, L., Umana, G., Trigilio, C., et al. 2017, MNRAS, 468, 3450
Cesaroni, R., Palagi, F., Felli, M., et al. 1988, A&AS, 76, 445
Christianto, H., & Seaquist, E.R. 1998, AJ, 115, 2466
Cho, S.-H., & Kim, J. 2010, ApJ, 719, 126
Claussen, M. J. Sahai, R., & Morris, M. R. 2009, ApJ, 691, 219
Cohen, M., Barlow, M. J., Liu, X.-W., et al. 2002, MNRAS, 332, 879
Condon, J. J., Cotton, W. D., Greisen, E. W., et al. 1998, AJ, 115, 1693
Cooper, H. D. B., Lumsden, S. L., Oudmaijer, R. D., et al. 2013, MNRAS, 430, 1125
Cox, P., Boulanger, F., Huggins, P. J., et al. 1998, ApJ, 495, L23
Dale, D. A., Bendo, G. J., Engelbracht, C. W., et al. 2005, ApJ, 633, 857
David, P., Le Squeren, A. M., & Sivagnanam, P. 1993, A&A, 277, 453
Dawson, J. R., Breen, S. L. GASKAP-OH Team 2024, in Cosmic Masers: Proper Motion toward the Next-Generation Large Projects, IAU Symp 380, eds. T. Hirota, H. Imai, K. Menten, Y. Pihlström (Cambridge: Cambridge University Press), 486
Day, F. M., Philström, Y. M., Claussen, M. J., et al. 2010, ApJ, 713, 986
de Gregorio-Monsalvo, I., Gómez, Y., Anglada, G., et al. 2004, ApJ, 601, 921
de Marco, O., & Soker, N. 2002, PASA, 114, 602
Deacon, R. M., Chapman, J. M., Green, A. J., et al. 2007, ApJ, 698, 1096
Decin, L., Homan, W., Danilovich, T., et al. 2019, NatAs, 3, 408
Deguchi, S., Matsunaga, N., & Fukushi, H. 2005, PASJ, 57, L25
Delgado-Inglada, G., Morisset, C., & Stasińska, G. 2014, MNRAS, 440, 536
DePoy, D. L., & Shields, J. C. 1994, ApJ, 422, 187
Desmurs, J. F., Baudry, A., Sivagnaman, P., et al. 2002, A&A, 394, 975
Desmurs, J. F., Baudry, A., Sivagnaman, P., et al. 2010, A&A, 520, A45
Diamond, P. J., Kemball, A. J., Junor, W., et al. 1994, ApJ, 430, L61
Duchesne, S. W., Grundy, J. A., Heald, G., et al. 2024, PASA, 41, 3
Dunham, M. M., Crapsi, A., Evans, N. J., et al. 2008, ApJS, 179, 249
Dunham, M. M., Arce, H. G., Allen, L. E., et al. 2013, AJ, 145, 94
Dzib, S. A., Yang, A. Y., Urquhart, J. S., et al. 2023, A&A, 670, A9
Eder, J., Lewis, B. M., & Terzian, Y. 1988, ApJS, 66, 183
Elitzur, M. 1992, ARA&A, 30, 75
Engels, D., & Bunzel, F. 2015, A&A, 582, A68
Engels, D. 2002, A&A, 388, 252
Fan, H., Nakashima, J. I., Engels, D., et al. 2024, ApJS, 270, 13
Ferland, G. J., Chatzikos, M., Guzmán, F., et al. 2017, Rev. Mex. Ast., 53, 385
Forster, J. R., & Caswell, J. L. 1989, A&A, 213, 339
Forster, J. R., & Caswell, J. L. 1999, A&AS, 137, 43
Franco, J., Tenorio-Tagle, G., & Bodenheimer, P. 1990, ApJ, 349, 126
Frew, D. J., Bojičić, I. S., & Parker, Q. A. 2013, MNRAS, 431, 2
García-Hernández, D. A., Manchado, A., García-Lario, P., et al. 2006, ApJ, 640, 829
García-Hernández, D. A., Perea-Calderón, J. V., Bobrowski, M., et al. 2007, ApJ, 666, L33
García-Rojas, J., Delgado-Inglada, G., García-Hernández, D. A., et al. 2018, MNRAS, 473, 4476
García-Segura, G., Taam, R. A., Ricker, P. M., et al. 2020, ApJ, 893, 150
Genzel, R., Lutz, D., Sturm, E., et al. 1998, ApJ, 498, 579
Gesicki, K., Zijlstra, A., Hajduk, M., et al. 2024, A&A, 689, A17
Ginsberg, A., Anderson, L. D., Dickey, S., et al. 2020, ApJS, 248, 24
Gledhill, T. M., & Forde, K. P. 2012, MNRAS, 421, 346
Gledhill, T. M., & Forde, K. P. 2015, MNRAS, 447, 1080
Gledhill, T. M., Forde, K. P., Lowe K. T. E., et al. 2011, MNRAS, 411, 1453
Gold, K. R., Schmidt, D. R., Ziurys, L. M., et al. 2024, ApJ, 976, 196
Gómez, Y., Moran, J. M., & Rodríguez, L. F. 1990, Rev. Mexicana Astron. Astrofis., 20, 55
Gómez, Y., Rodríguez, L. F., Contreras, M. E., & Moran, J. M. 1994, Rev. Mexicana Astron. Astrofis., 28, 97
Gómez, J. F., de Gregorio-Monsalvo, I., Lovell, J. E. J., et al. 2005, MNRAS, 364, 738
Gómez, J. F., Suárez, O., Gómez, Y., et al. 2008, AJ, 135, 2074
Gómez, J. F., Rizzo, R., Suárez, O., Miranda, L. F., et al. 2011, ApJ, 739, L14
Gómez, J. F., Rizzo, J. R., Suárez, O., et al. 2015a, A&A, 578, A119
Gómez, J. F., Suárez, O., Bendjoya, P., et al. 2015b, ApJ, 799, 186
Gómez, J. F., Uscanga, L., Green, J. A., et al. 2016, MNRAS, 461, 3259
Gómez, J. F., Suárez, O., Rizzo, J. R., et al. 2017, MNRAS, 468, 2081
Gómez, J. F., Nicollini, G., Suárez, O., et al. 2018a, MNRAS, 480, 4991
Gómez, J. F., Miranda, L. F., Uscanga, L., et al. 2018b, in Astrophysical Masers: Unlocking the Mysteries of the Universe, Proceedings of the International Astronomical Union, IAU Symp 336, eds. A. Tarchi, M. J Reid, P. Castangia (Cambridge: Cambridge University Press), 377
Gómez, J. F., Imai, H., Uscanga, L., et al. 2023, in Highlights of Spanish Astrophysics XI, Proceedings of the XV Scientific Meeting of the Spanish Astronomical Society, eds. M. Manteiga, L. Bellot, P. Benavidez, et al., 210
Gordon, Y. A., Boyce, M. M., O'Dea, C. P., et al. 2021, ApJS, 255, 30
Gruenwald, R., & Aleman, A. 2007, A&A, 461, 1019
Hajduk, M., Todt, H., Hamann, W.-R., et al. 2020, MNRAS, 498, 1205
Hale, C. L., McConnell, D., Thomson, A. J. M., et al. 2021, PASA, 38, 58
Hambly, N. C., Collins, R. S., Cross, N. J. G., et al. 2008, MNRAS, 384, 637
Helfand, D. J., Zoonematkermani, S., Becker, R. H., et al. 1992, ApJS, 80, 211
Herman, J., & Habing, H. J. 1985, A&AS, 59, 523
Hewett, P. C., Warren, S. J., Leggett, S. K., et al. 2006, MNRAS, 367, 454
Hofner, P., & Churchwell, E. 1996, A&AS, 120, 283
Houck, J. R., Roellig, T. L., van Cleve, J., et al. 2004, ApJS, 154, 18
Hrivnak, B. J., Kwok, S., Geballe, T. R., et al. 1994, ApJ, 420, 783
Hsia, C. K., Kwok, S., Zhang, Y., et al. 2010, ApJ, 725, 173
Imai, H., Obara, K., Diamond, P. J., et al. 2002, Nature, 417, 829
Imai, H., Morris, M. R., Sahai, R., et al. 2004, A&A, 420, 265
Imai, H., Nakashima, J. I., Kwok, S., et al. 2013, ApJ, 773, 182
Imai, H., Hamae, Y., Amada, K., et al. 2023, PASJ, 75, 1183
Irabor, T., Hoare, M. G., Oudmaijer, R. D., et al. 2018, MNRAS, 480, 2423
Irabor, T., Hoare, M. G., Burton, M., et al. 2023, MNRAS, 520, 1073
Ivanova, N., Justham, S., Chen, X., et al. 2013, A&A Rev, 21, 59
Jacoby, G. H., & Van de Steene, G. 2004, A&A, 419, 563
Jewell, P. R., Schenewerk, M. S., & Snyder, L. E. 1985, AJ, 295, 183
Kahn, F. D. 1954, Bull. Astron. Inst. Netherlands, 12, 187
Kanarek, G., Shara, M., Faherty, J., et al. 2015, MNRAS, 452, 2858
Kimeswenger, S. 2001, Rev. Mex. Ast., 37, 115
Kohoutek, L. 2001, A&A, 378, 846
Khouri, T., Vlemmings, W. H. T., Tafoya, D., et al. 2021, NatAs, 6, 275
Kwok, S., Purton, C. R., & Keenan, D. W. 1981, ApJ, 250, 232
Ladeyschikov, D. A., Bayandina, O. S., & Sobolev, A. M. 2019, AJ, 158, 233
Lawrence, A., Warren, S. J., Almaini, O., et al. 2007, MNRAS, 379, 1599
Lebzelter, T., Mowlavi, N., Lecoeur-Taibi, I., et al. 2023, A&A, 674, A15

[2] http://www.astropy.org

Lewis, B. M. 1994, ApJS, 93, 549
Lewis, B. M., & Araújo, F. X. 1989, ApJ, 338, 234
Likkel, L. 1989, ApJ, 344, 350
Loup, C., Forveille, T., Nyman, L. A., et al. 1990, A&A, 227, L29
Lumsden, S. L., Puxley, P. J., & Hoare, M. G. 2001a, MNRAS, 320, 83
Lumsden, S. L., Puxley, P. J., & Hoare, M. G. 2001b, MNRAS, 328, 419
Lyu, J., & Rieke, G., 2022, Universe, 8, 304
Manchado, A., Guerrero, M. A., Stanghellini, L., & Serra-Ricart M. 1996, The IAC morphological catalog of northern Galactic planetary nebulae (La Laguna, Spain: Instituto de Astrofisica de Canarias (IAC))
Manchado, A., Stanghellini, L., Villaver, E., et al. 2015, ApJ, 808, 115
Marcolino, W. L. F., & Araújo, F. X. 2003, AJ, 126, 887
Márquez-Lugo, R. A., Ramos-Larios, G., Guerrero, M., et al. 2013, MNRAS, 429, 973
Márquez-Lugo, R. A., Kemp, S. N, Ramos-Larios, G. et al. 2024, Rev. Mex. Astron. Astrofis., 60, 261
Maron, O., Kijak, J., Kramer, M., & Wielebinski, R., 2000, A&AS, 147, 195
Martín-Hernández, N. L., Vermeij, R., Tielens, A. G. G. M., et al. 2002, A&A, 389, 286
Matsuura, M., Bernard-Salas, J., Lloyd Evans, T., et al. 2019, MNRAS, 439, 1472
Medina, S.-N. X., Urquhart, J. S., Dzib, S. A., et al. 2019, A&A, 627, A175
Menten K. M., Wyrowski F., Keller D., et al. 2018, A&A, 613, A49
Menzies, J. W., & Wolstencroft, R. D. 1990, MNRAS, 247, 177
Miller Bertolami, M. M. 2016, A&A, 588, A25
Miranda, L. F., Fernández, M., Alcalá, J. M., et al. 2000, MNRAS, 311, 748
Miranda, L. F., Gómez, Y., Anglada, G., et al. 2001, Nature, 414, 284
Miranda, L. F., Suárez, O., Olguín, L., et al. 2021, arXiv e-prints [arXiv:2105.05186]
Monet D. G., Levine, S. E., Canzian, B., et al. 2003, AJ, 125, 984
Morisset, C., Delgado-Inglada, G., & Flores-Fajardo, N. 2015, Rev. Mex. Astron. Astrofis., 51, 101
Murphy, T., Sadler, E. M., Ekers, R. D., et al. 2010, MNRAS, 402, 2403
Norris, R. P., Allen, D. A., Haynes, R. F., et al. 1984, PASA, 5, 562
Ogbodo, C. S, Green, J. A., Dawson, J. R., et al. 2020, MNRAS, 493, 199
Olnon, F. M. 1975, A&A, 39, 217
Orosz, G., Gómez, J. F., Imai, H., et al. 2019, MNRAS, 482, L40
Ortega, M. E., Petriella, A., & Paron, S. 2024, MNRAS, 532, 4446
Ortiz-León, G. N., Menten, K. M., Kamiński, T., et al. 2020, A&A, 638, A17
Oudmaijer, R. D., Waters, L. B. F. M., van der Veen, W. E. C. J., et al. 1995, A&A, 299, 69
Ouyang, X.-J., Zhang, Y., Zhang, C.-P., et al. 2024, ApJ, 972, 96
Panagia, N., & Felli, M. 1975, A&A, 39, 1
Parker, Q. A., Bojičić, I. S., Frew, D. J., et al. 2016, JPhCs, 728, 3
Parthasarathy, M., Acker, A., & Stenholm, B. 1998, A&A, 329, L9
Payne, H. E., Phillips, J. A., & Terzian, Y. 1988, ApJ, 326, 368
Peeters, E., Spoon, H. W. W., & Tielens, A. G. G. M. 2004, ApJ, 613, 986
Pérez-Sántaella, M., Diamond-Stanic, A. M., Alonso-Herrero, A., et al. 2010, MNRAS, 725, 2270
Pérez-Sánchez, A. F., Vlemmings, W. H. T., & Chapman, J. M. 2011, MNRAS, 418, 1402
Pérez-Sánchez, A. F., Vlemmings, W. H. T., Tafoya, D., et al. 2013, MNRAS, 436, L79
Pérez-Sánchez, A. F., Tafoya, D., García López, R., et al. 2017, A&A, 601, A68
Preite-Martinez, A. 1988, A&AS, 76, 317
Pottasch, S. R., Bignelli, C., & Zijlstra, A. 1987, A&A, 177, L49
Pottasch, Dennefeld, M., & Mo, J. 1986, A&A, 155, 397
Popescu, C. C., Tuffs, R. J., Dopita, M. A. 2011, A&A, 527, A109
Purcell, C. R., Hoare, M. G., Cotton, W. D., et al. 2013, ApJS, 205, 1
Qiao, H.-H., Walsh, A. J., Gómez, J. F., et al. 2016a, ApJ, 817, 37
Qiao, H.-H., Walsh, A. J., Green, J. A., et al. 2016b, ApJS, 227, 26
Qiao, H.-H., Walsh, A. J., Breen, S. L., et al. 2018, ApJS, 239, 15
Qiao, H.-H., Breen, S. L., Gómez, J. F., et al. 2020, ApJS, 247, 5
Ramos-Larios, G., Guerrero, M. A., Suárez, O., et al. 2009, A&A, 501, 1207
Ramos-Larios, G., Guerrero, M. A., Suárez, O., et al. 2012, A&A, 545, A20
Rayner, J. T., Cushing, M. C., & Vacca, W. D. 2009, ApJS, 185, 289
Reid M. J., & Moran J. M. 1981, ARA&A, 19, 231
Reynolds, S. P. 1986, ApJ, 304, 713
Rizzo, J. R., Gómez, J. F., Miranda, L. F., et al. 2013, A&A, 560, A82
Robitaille, T. P., Whitney, B. A., Indebetouw, R., et al. 2007, ApJS, 169, 328
Sabin, L., Parker, Q. A., Corradi, R. L. M., et al. 2014, MNRAS, 443, 3388
Schmidt, D. R., & Ziuris , L. M. 2019, ApJ, 881, L38
Seaquist, E. R., & Davis, L. E. 1983, ApJ, 274, 659
Seaquist, E. R., Ivison, R. J., & Hall, P. J. 1995, MNRAS, 276, 867
Sevenster, M. N., Chapman, J. M., Habing, H. J., et al. 1997, A&AS, 122, 79
Sevenster, M. N. 2002, AJ, 123, 2772
Sheperd, M. C., Cohen, R. J., Gaylard, M. J., & West, M. E. 1990, Nature, 344, 522
Simpson, J. P., Cotera, A. S., Burton, M. G., et al. 2012, MNRAS, 419, 211
Suárez, O., García-Lario, P., Manchado, A., et al. 2006, A&A, 458, 173
Suárez, O., Gómez, J. F., & Miranda, L. F., 2008, ApJ, 689, 430
Suárez, O., Gómez, J. F., Miranda, L. F, et al. 2009, A&A, 505, 217
Suárez, O., Gómez, J. F., Bendjoya, P., et al. 2015, ApJ, 806, 105
Surendiranath, R. 2002, A&A, 390, 667
Sutherland, R. S., & Dopita, M. A. 2017, ApJS, 229, 34
Szabó, Zs. M., Belloche, A., Menten, K. M., et al. 2025, A&A, 694, A329
Szczerba, R., Siódmak, N., Stasińska, G., et al. 2007, A&A, 469, 799
Szymczak, M., & Gérard, E. 2004, A&A, 423, 209
Tafoya, D., Gómez, Y., Anglada, G., et al. 2007, ApJ, 133, 364
Tafoya, D., Gómez, Y., Patel, N. A., et al. 2009, AJ, 691, 611
Tafoya, D., Imai, H., Gómez, J. F., et al. 2020, ApJ, 890, L14
Taylor, A. R., Pottasch, S. R., & Zhang, C. Y. 1987, A&A, 171, 178
Tylenda, R., Acker, A., & Stenholm, B., 1993, A&AS, 102, 595
te Lintel Hekkert, P., & Chapman, J., 1996, A&AS, 119, 459
te Lintel Hekkert, P., Versteeg-Hensel, H. A., Habing, H. J., et al. 1989, A&AS, 78, 399
te Lintel Hekkert, P., Caswell, J. L., Habing, H. J., et al. 1991, A&AS, 90, 327
Urquhart, J. S., Busfield, A. L., Hoare, M. G., et al. 2008, A&A, 487, 253
Urquhart, J. S., Hoare, M. G., Purcell, C. R., et al. 2009, A&A, 501, 539
Urquhart, J. S., Morgan, L. K., Figure, C. C., et al. 2011, MNRAS, 418, 1689
Uscanga, L., Gómez, J. F., Suárez, O., et al. 2012, A&A, 547, A40
Uscanga, L., Gómez, J. F., Miranda, L. F., et al. 2014, MNRAS, 444, 217
Uscanga, L., Imai, H., Gómez, J. F., et al. 2023, ApJ, 948, 17
Van de Steene, G. C., & Pottasch, S. R. 1995, ApJ, 299, 238
Vassiliadis, E., & Wood, P. R. 1994, ApJS, 92, 125
Vyssotsky, A. N., Miller, W. J., & Walther, M. E., 1945, PASP, 57, 314
Vlemmings, W. H. T., Amiri, N., & van Langevelde, H. J. 2014, A&A, 569, A92
Walsh, A. J., Breen, S. L., Bains, I., et al. 2009, MNRAS, 394, L70
Walsh, A. J., Purcel, C. R., Longmore, S. N., et al. 2014, MNRAS, 442, 2240
Wang, Y., Bihr, S., Rugel, M., et al. 2018, A&A, 619, A124
Wardle, M., & Yusef-Zadeh, F. 2002, Science, 296, 2350
Weaver, K. A., Meléndez, M., Mushotzky, R. F., et al. 2010, ApJ, 716, 1151
Weidmann, W. A., Méndez, R. H., & Gamen, R. 2015, A&A, 579, A86
Weidmann, W. A., Mari, M. B., Schmidt, E. O., et al. 2020, A&A, 640, A10
White, R. L., Becker, R. H., & Helfand, D. J. 2005, AJ, 130, 586
Whitelock, P., & Menzies, J. W. 1986, MNRAS, 223, 497
Wong, K. T., Menten, K. M., Kamiński, T., et al. 2018, A&A, 612, A48
Wood, D. O. S., & Churchwell, E. 1989, ApJ, 340, 265
Xu, Y., Reid, M. J., Menten, K. M., et al. 2006, ApJS, 166, 526
Yoon, D.-H., Cho, S.-H., Kim, J., et al. 2014, ApJS, 211, 15
Yung, B. H. K., Nakashima, J.-I., Imai, H., et al. 2011, ApJ, 741, 94
Yung, B. H. K., Nakashima, J.-I., Imai, H., et al. 2013, ApJ, 769, 20
Yung, B. H. K., Nakashima, J.-I., & Henkel, C., 2014, ApJ, 794, 81
Zhang, C. Y., & Kwok, S. 1991, A&A, 250, 179
Zijlstra, A. A., te Lintel Hekkert, P., Pottasch, S. R., et al. 1989, A&A, 217, 157
Zijlstra, A. A., Gaylard, M. J., te Lintel Hekkerd, P., et al. 1991, A&A, 243, L9
Zijlstra, A. A., Chapman, J. M., te Lintel Hekkerd, P., et al. 2001, MNRAS, 322, 280
Zoonematkermani, S., Helfand, D. J., Becker, R. H., et al. 1990, ApJS, 74, 181
Zou, Y., Frank, A., Chen, Z., et al. 2020, MNRAS, 497, 2855

Appendix A: Parameters of the ATCA and VLA observations

Table A.1 shows the final list of observed targets, as well as the main parameters of our radio interferometric observations.

Table A.1: Parameters of the ATCA/VLA observations.

Target name	Date	Band	Phase calibrator	Synthesized beam[a]		rms[b]	Telescope
				(arcsec)	(deg)	(mJy beam^{-1})	
IRAS 07027−7934	2020/10/19	L	PKS 0606-796	5.2 × 3.3	+72	13	ATCA
IRAS 14079−6402	2020/10/19	L	PMN J1355-6326	6.1 × 3.0	−22	42	ATCA
IRAS 14086−6907	2020/10/19	L	PMN J1355-6326	5.9 × 3.0	−22	45	ATCA
IRAS 15559−5546	2020/10/19	L	PMN J1650-5044	6.1 × 3.3	−40	34	ATCA
IRAS 16280−4008	2020/10/19	L	PMN J1650-5044	8.5 × 3.5	−42	29	ATCA
IRAS 17180−2708	2020/10/20	L	PKS 1657-261	8.0 × 3.6	−5	59	ATCA
	2021/04/03	L	J1700-2610	107 × 32	−21	39	VLA
	2021/04/01	K	J1700-2610	6.2 × 2.2	−23	9	VLA
IRAS 17221−3038	2020/10/20	L	PMN J1733-3722	7.9 × 3.4	−4	38	ATCA
IRAS 17253−2824	2020/10/20	L	PKS 1657-261	7.5 × 3.7	+5	33	ATCA
	2021/04/03	L	J1700-2610	110 × 31	−18	23	VLA
	2021/04/01	K	J1700-2610	6.4 × 2.1	−21	7	VLA
IRAS 17374−2700	2020/10/20	L	PKS 1657-261	8.6 × 3.4	−8	33	ATCA
	2021/04/03	L	J1700-2610	118 × 30	−22	24	VLA
	2021/04/01	K	J1700−2610	6.0 × 2.1	−20	8	VLA
IRAS 17385−2211	2020/10/20	L	1808-209	9.0 × 3.4	−1	16	ATCA
	2021/04/03	L	J1700-2610	89 × 32	−20	23	VLA
	2021/04/01	K	J1733-1304	4.9 × 2.5	−13	13	VLA
IRAS 17403−2107	2020/10/20	L	1808-209	9.6 × 3.3	−2	40	ATCA
	2021/04/03	L	J1700-2610	83 × 33	−14	38	VLA
	2021/04/01	K	J1733-1304	4.6 × 2.2	−13	11	VLA
IRAS 17487−1922	2020/10/20	L	1808-209	12.6 × 3.3	−2	80	ATCA
	2021/04/03	L	J1700-2610	79 × 39	−15	10	VLA
	2021/04/01	K	J1733-1304	4.3 × 2.2	−12	12	VLA
IRAS 17494−2645	2021/04/01	K	J1820-2528	5.8 × 2.2	−20	8	VLA
IRAS 18019−2216	2021/04/01	K	J1820-2528	5.1 × 2.2	−20	10	VLA
IRAS 18243−1048	2020/10/19	L	1819-096	18.8 × 3.7	−1	12	ATCA
IRAS 18271−1014	2020/10/19	L	1819-096	20.3 × 3.5	0	11	ATCA
	2021/04/03	L	J1700-2610	63 × 33	−18	20	VLA
	2021/04/01	K	J1832-1035	3.9 × 2.4	−17	9	VLA
IRAS 18295−2510	2020/10/20	L	1808-209	9.6 × 3.4	−7	39	ATCA
	2021/04/03	L	J1700-2610	99 × 31	−19	60	VLA
	2021/04/01	K	J1820-2528	5.2 × 2.2	−15	14	VLA
OH 25.646−0.003	2021/03/25	K	J1832-1035	3.7 × 2.4	−26	12	VLA
IRAS 18443−0231	2021/04/03	L	J1822-0938	52 × 35	0	75	VLA
	2021/03/25	K	J1851+0035	4.2 × 3.3	−14	8	VLA
IRAS 18480+0008	2021/03/25	K	J1851+0035	3.4 × 2.4	−23	7	VLA
IRAS 18508+0047	2021/03/25	K	J1851+0035	3.4 × 2.4	−21	12	VLA
IRAS 18551+0159	2021/04/03	L	J1822-0938	51 × 33	−11	70	VLA
	2021/03/25	K	J1851+0035	3.3 × 2.4	−21	14	VLA
IRAS 19035+0801	2020/10/19	L	1910+052	30.2 × 3.4	0	10	ATCA
	2021/03/25	L	J1925+2106	49 × 35	−6	27	VLA
	2021/03/25	K	J1851+0035	3.1 × 2.4	−21	13	VLA
IRAS 19123+1139	2020/10/19	L	1910+052	30.2 × 3.4	0	29	ATCA
	2021/03/25	L	J1925+2106	47 × 35	−6	75	VLA
	2021/03/25	K	J1924+1540	2.9 × 2.4	−17	12	VLA
IRAS 19127+1717	2020/10/19	L	1910+052	25.8 × 3.2	+2	20	ATCA
	2021/03/25	L	J1925+2106	46 × 36	−3	30	VLA
	2021/03/25	K	J1924+1540	2.8 × 2.4	−13	11	VLA
IRAS 19194+1548	2021/03/25	K	J1924+1540	2.8 × 2.4	−14	11	VLA
IRAS 19200+1035	2020/10/19	L	1910+052	22.7 × 3.4	0	30	ATCA
	2021/03/25	L	J1925+2106	48 × 35	−7	30	VLA
	2021/03/25	K	J1924+1540	3.0 × 2.4	−15	12	VLA
IRAS 19508+2659	2021/03/25	K	J2023+3153	3.5 × 2.6	−71	12	VLA
IRAS 20266+3856	2021/04/03	L	J2025+3343	43 × 33	+27	70	VLA
	2021/03/25	K	J2015+3710	3.7 × 2.5	−83	15	VLA

Notes. [a] Major and minor axes and position angle of the synthesized beam of continuum images. [b] Noise level, measured at the channel map with the weakest maser. If there is no detection, measured at the position and channel map with the V_{LSR} of the reported OH maser from single-dish observations.

Appendix B: Further details of our results

Appendix B.1: Targets with positional association between maser and radio continuum in our ATCA/VLA observations

In Table B.1 we show the interferometric positions of the radio continuum and maser emission of the matches we found, as well as the angular distance between the two types of emission (δ). In some cases, these spatial matches were obtained from the positions reported in literature data. Moreover, our interferometric ATCA/VLA observations allowed us to upgrade the status of several of the sources labeled SC or SP in Table 1 to either IC or IP. In order to report the specific maser species involved, IP sources (confirmed maser-emitting PNe) are shown in Table B.1 as OHPNe and/or H_2OPNe in the "nature" column. For IC sources (candidate maser-emitting PNe) we use the same labels, but enclosed by parentheses. Similarly, we label water fountain sources as WF, and WF candidates as WF, but enclosed by parenthesis.

Appendix B.2: Details of individual maser components

In Tables B.2 to B.8 we present the parameters of the spectral components of masers, in the sources where there is more than one such component. In sources with a single maser component, relevant information is already given in Table B.1. For each maser component, we indicate its position (right ascension and declination), their positional uncertainties ($\delta_{\rm R.A.}$, $\delta_{\rm dec}$), the observed transition (H_2O at 22235 MHz, or OH at 1612, 1665, 1667, and 1720 MHz), LSR velocity ($V_{\rm LSR}$) in km s^{-1}, and peak flux density (S_ν) in Jy. In most cases, the masers components in these tables were obtained from the observations reported in this paper, but we have also added values from the literature, when relevant.

We note that the reported positional uncertainties are those obtained with a fit of an elliptical Gaussian to the image of the channel with the peak emission of each component. These are to be understood as relative errors among the components of an individual maser transition and observational epoch. To compare positions between different epochs and transitions, one should consider the uncertainties in absolute astrometry, which are typically on the order of 10% of the synthesized beam.

Appendix B.3: Targets without positional association between maser and radio continuum in our ATCA/VLA observations

In Table B.9 we report the cases for which maser and continuum emission were both detected in our field of view, but their position did not match, and a careful analysis indicates that the emission of each type arises from different sources, and thus we can discard them as possible maser-emitting PNe. Each of these sources are described in the subsections B.3.1 to B.3.6 of this appendix.

Table B.10 shows the sources in which continuum and/or maser emission was not detected. Given the possible variability of the sources, in those cases we cannot discard nor confirm that the previously reported emission of these types was actually associated, but one or both of them fell below our sensitivity threshold. We note that we also included the source OH 25.646−0.003 in that table, although it is a confirmed OHPN candidate, but we show there our non-detection of H_2O masers at 22 GHz, and of continuum emission around that frequency.

Appendix B.3.1: The field of IRAS 14086−6907

OH maser emission was first reported toward IRAS 14086−6907 from single-dish observations by te Lintel Hekkert et al. (1991). Radio continuum emission (source RACS-DR1 J141249.8-692104) was detected with the ASKAP interferometer near this object (Hale et al. 2021). The radio continuum position is ∼7″ away from the source 2MASS J14125041-6921092, which is the near-infrared counterpart of IRAS 14086−6907. We have detected both OH masers and radio continuum emission in our interferometer observations. We confirm that the OH maser emission is associated with the AGB star IRAS 14086−6907 (Lebzelter et al. 2023), and is indeed separated from the continuum emission by ∼7″. The parallax of the Gaia source associated with IRAS 14086−6907 (Gaia DR3 5846602400091413632) indicates it is at a distance of ≃1 kpc. The separation of the radio continuum emission would correspond to 7000 au at this distance. We can confidently discard that the presence of this radio continuum emission could indicate that IRAS 14086−6907 is a PN, since we would not expect unresolved radio continuum emission that far away from the central star without any hint of emission closer to it. The nature of the radio continuum emission is unknown, but it is probably associated to an extragalactic object, since it is brighter at 887.5 MHz (Hale et al. 2021) than at 1367.5 MHz (Duchesne et al. 2024), suggesting non-thermal emission. A possible optical counterpart for the radio continuum source is Gaia DR3 5846602404392109312.

Appendix B.3.2: The field of IRAS 15559−5546

IRAS 15559−5546 (Hen 2-142) has been spectroscopically classified as a PN (Frew et al. 2013). OH maser emission with a double-peaked spectral profile has been reported in its neighborhood with single-dish observations (te Lintel Hekkert et al. 1991). We have detected both radio continuum and OH maser emission within the observed field, with a separation between them of ∼2.4 arcmin. The radio continuum emission is clearly associated with the PN IRAS 15559−5546, while the OH masers are emitted by IRAS 15557−5546 (Sevenster et al. 1997), which has been previously classified as an AGB star (Sevenster 2002). We did not detect any radio continuum emission from IRAS 15557−5546.

Appendix B.3.3: The field of IRAS 17385−2211

IRAS 17385−2211 has been spectroscopically classified as PN (Frew et al. 2013). Double-peaked 1612 MHz OH maser emission was reported in its neighborhood based on single-dish observations (te Lintel Hekkert et al. 1991). We have detected the radio continuum emission from the PN. However, the position of the OH maser emission coincides with that of IRAS 17388−2203, which has been spectroscopically classified as a post-AGB star (Suárez et al. 2006), and it is ∼8.3 arcmin away from IRAS 17385−2211. We confirm the association of OH maser emission from this post-AGB star for the first time. The maser spectrum displays multiple emission features, whose velocities coincide with those seen in the single-dish spectrum reported by te Lintel Hekkert et al. (1991). We did not detect any radio continuum emission at 2.1 GHz from IRAS 17388−2203.

Appendix B.3.4: The field of IRAS 18243−1048

Double-peaked 1612 MHz OH maser emission was reported by single-dish observations towards IRAS 18243−1048

Table B.1: Characteristics of the radio continuum, H_2O and OH maser emission of the maser-emitting PNe and candidates studied in this paper.

	Radio continuum emission			Maser emission				
Source	Position RA, DEC (J2000)	Frequency (GHz)	Flux density (mJy)	Position RA, DEC (J2000)	Transition	δ^a ($''$)	Flux density (Jy)	Nature^b
From our observations								
IRAS 07027−7934	06:59:26.327 −79:38:47.02	2.1	5.37±0.28	06:59:26.273 −79:38.46.99	OH 1612 MHz	0.15±0.04	0.602±0.016	OHPN
IRAS 17487−1922	17:51:44.868 −19:23:42.26	2.1	0.68±0.18	17:51:44.981 −19:23:40.21	OH 1612 MHz	2.6±1.8	0.44±0.07	(OHPN)
		1.5	<1.45	17:51:44.645 −19:23:38.67	OH 1612 MHz	5±9	0.52±0.05	
IRAS 18443−0231	18:47:00.4017 −02:27:52.573	22.2	226.3±0.4	18:47:00.4012 −02:27:52.552	H_2O 22 GHz	0.022±0.009	9.80±0.03	(H_2OPN), WF
IRAS 19035+0801	19:05:56.436 +08:06:56.88	2.1	2.63±0.22	19:05:56.413 +08:06:57.86	OH 1612 MHz	1.0±0.4	0.364±0.019	(OHPN)
		1.5	0.93±0.09	19:05:56.289 +08:06:56.17	OH 1612 MHz	2.3±5.9	0.857±0.019	
From our observations and the literature								
IRAS 18019−2216^c	18:04:57.359 −22:15:50.84	22.2	0.583±0.018	18:04:57.347 −22:15:50.91	H_2O 22 GHz	0.18±0.26	0.332±0.010	(H_2OPN), WF
IRAS 18480+0008^d	18:50:36.659 +00:12:28.25	3.0	1.90±0.22	18:50:36.685 +00:12:28.34	OH 1665 MHz	0.4±1.9	0.116±0.009	(OHPN)
	18:50:36.659 +00:12:28.13	22.2	2.020±0.013	18:50:36.6614 +00:12:28.191	H_2O 22 GHz	0.071±0.020	1.957±0.014	(H_2OPN), (WF)
From the literature								
IRAS 16029−5055	16:06:40.60 −51:03:57.2	5.5	3.02±0.15	16:06:40.637 −51:03:55.73	OH 1612 MHz	1.5±0.9	1.31±0.13	(OHPN)
IRAS 18213−1245A	18:24:09.722 −12:43:22.84	4.8	3.6±0.8	18:24:09.727 −12:43:23.90	OH 1665 MHz	1.1±1.0	0.139±0.005	(OHPN)
				18:24:09.706 −12:43:24.04	H_2O 22 GHz	1.22±1.41	3.70±0.04	(H_2OPN)
IRAS 18464−0140	18:48:56.647 −01:36:42.98	3.0	4.8±0.4	18:48:56.523 −01:36:43.32	OH 1612 MHz	1.9±1.9	1.749±0.021	(OHPN)
				18:48:56.62 −01:36:44.3	OH 1665 MHz	1.4±1.7	0.500±0.010	
				18:48:56.523 −01:36:42.99	OH 1667 MHz	1.9±1.5	1.90±0.010	
				18.48.56.65 −01.36.43.04	H_2O 22 GHz	0.1±0.4	16.11±0.14	(H_2OPN), WF
IRAS 18508+0047	18:53:22.196 +00:50:49.03	1.4	2.58±0.22	18:53:22.29 +00:50:48.46	OH 1612 MHz	1.5±1.9	0.529±0.005	(OHPN)
IRAS 19176+1251	19:19:55.744 +12:57:37.70	1.5	3.01±0.28	19:19:55.850 +12:57:37.80	OH 1720 MHz	1.6±0.4	0.115±0.003	(OHPN)
IRAS 19194+1548	19:21:40.374 +15:53:55.16	1.5	3.23±0.26	19:21:40.514 +15:53:54.74	OH 1612 MHz	2.1±1.2	0.917±0.008	OHPN
				19:21:40.286 +15:53:46.39	OH 6035 MHz	8.86±1.12	4.80±0.11	
OH 25.646−0.003	18:38:06.242 −06:28:51.22	5	2.21±0.04	18:38:06.165 −06:28:54.10	OH 1612 MHz	3.1±1.9	0.254±0.005	(OHPN)

Notes: ^{a} Relative distance between the radio continuum emission peak and the maser spot. ^{b} In parenthesis sources candidates to PN or candidate to WF. WF: water fountain characteristics. ^{c} This source is a previously reported OHPN candidate (Cala et al. 2022). ^{d} The flux density at 3 GHz was reported in VLASS (Gordon et al. 2021), and the 1665 MHz was reported in THOR (Beuther et al. 2019).

Table B.2: OH maser emission in our ATCA observations of IRAS 07027−7934.

Maser coordinates		$\delta_{\rm R.A.}$	$\delta_{\rm dec}$	Transition	$V_{\rm LSR}$	S_ν
R.A.(J2000)	Dec(J2000)	(arcsec)	(arcsec)	(MHz)	(km s^{-1})	(Jy)
06:59:26.273	−79:38:46.99	0.04	0.05	1612	−46.45	0.646±0.027
06:59:26.780	−79:38:47.54	0.22	0.21	1612	−40.28	0.30±0.04
06:59:25.218	−79:38:49.04	0.24	0.24	1612	−41.37	0.173±0.031

Table B.3: OH maser emission in our ATCA and VLA observations of IRAS 17487−1922

Maser coordinates		$\delta_{\rm R.A.}$	$\delta_{\rm dec}$	Transition	$V_{\rm LSR}$	S_ν
R.A.(J2000)	Dec(J2000)	(arcsec)	(arcsec)	(MHz)	(km s^{-1})	(Jy)
17:51:44.89120	−19:23:46.8	0.0020	0.4	1612	−39.18	0.39±0.07
17:51:44.79420	−19:23:46.66	0.0013	0.20	1612	−39.00	0.41±0.04
17:51:44.9810	−19:23:41.91	0.015	0.24	1612	−38.82	0.44±0.05
17:51:44.91960	−19:23:40.9	0.0019	0.4	1612	−38.64	0.44±0.09
17:51:44.8501	−19:23:46.8	0.004	0.6	1612	−38.37	0.345±0.011
17:51:44.98140	−19:23:40.21	0.0020	0.31	1612	−38.10	0.44±0.07
17:51:45.12	−19:23:42.9	0.4	0.4	**1612**	−38.15	0.58±0.05
17:51:44.711	−19:23:43.41	0.21	0.21	**1612**	−39.06	0.48±0.08
17:41:45.36	−19:23:42.0	0.3	0.4	**1612**	−39.60	0.38±0.04

Notes. The VLA observations are marked with the frequency of the transition in boldface. The ones with normal fonts, represent the ATCA observations

Table B.4: H_2O maser emission in our VLA observations of IRAS 18019−2216.

Maser coordinates		$\delta_{\rm R.A.}$	$\delta_{\rm dec}$	Transition	$V_{\rm LSR}$	S_ν
R.A.(J2000)	Dec(J2000)	(arcsec)	(arcsec)	(MHz)	(km s^{-1})	(Jy)
18:34:57.3719	−22:15:50.65	0.005	0.24	22235	−10.11	0.194±0.017
18:34:57.3520	−22:15:50.8	0.013	0.4	22235	−4.63	0.111±0.020
18:34:57.3472	−22:15:50.92	0.006	0.21	22235	−1.47	0.222±0.013
18:34:57.3511	−22:15:50.23	0.005	0.18	22235	+3.37	0.167±0.013
18:34:57.3468	−22:15:50.91	0.003	0.11	22235	+5.90	0.332±0.010
18:34:57.3365	−22:15:51.17	0.004	0.14	22235	+8.01	0.247±0.008

(te Lintel Hekkert et al. 1991). There is a radio continuum source located ∼ 20" away from this infrared source, whose emission has been reported at different frequencies (e.g., Condon et al. 1998; Purcell et al. 2013), and that lies within the beam of the OH single-dish observations. Our interferometric observations detect both the OH maser and radio continuum emission in the field, and we can confirm that the OH maser emission is indeed associated with IRAS 18243−1048 (2MASS J18270824-1046099), ∼ 20" away from the radio continuum source. The position of the latter is located next (∼ 2" away) to a different infrared source in 2MASS (source 2MASS J18270688-1046087) and Spitzer (source SSTGLMC G020.5893+00.4247) images, with no extended emission connecting it with IRAS 18243−1048.

Appendix B.3.5: The field of IRAS 18295−2510

IRAS 18295−2510 (NGC 6644) is a spectroscopically classified PN (e.g., Frew et al. 2013). The possible association of this PN with OH maser emission at 1612 MHz had been previously suggested by Zijlstra et al. (1989), based on single-dish observations. We have detected the radio continuum emission from the the PN. We also found double-peaked OH maser emission in the field, but it arises from a different source, IRC 20491, located ≃2′ away from NGC 6644.

Appendix B.3.6: The field of IRAS 19200+1035

Double-peaked 1612 MHz OH maser-emission has been reported towards IRAS 19200+1035 based on single-dish observations (Eder et al. 1988). The position of this source (associated to 2MASS 19222483+1040506) lies ∼41″ away from the spectroscopically confirmed PN K 3-33, so both objects fall within the beam of the OH maser observations. In our data, we have detected the radio continuum emission from the PN. We have also detected OH maser emission in the field, but it is not associated with either PN K 3-33 or IRAS 19200+1035, but with the source IRAS 19201+1040 (2MASS J19222916+1046200) instead, an object which is ∼5 arcmin away from PN K 3-33. This same double-peaked OH maser emission has also been reported in IRAS 19201+1040 (e.g., Lewis 1994), and ours is the first interferometric detection of this emission, which allows us to properly associate it to IRAS 19201+1040, rather than to IRAS 19200+1035. We have not detected any radio continuum emission from IRAS 19201+1040.

Table B.5: H_2O maser emission (our VLA observations) and OH (from the literature) maser emission of IRAS 18480+0008.

Maser coordinates		$\delta_{R.A.}$	δ_{dec}	Transition	V_{LSR}	S_ν
R.A.(J2000)	Dec(J2000)	(arcsec)	(arcsec)	(MHz)	(km s^{-1})	(Jy)
18:50:36.685	+00:12:28.34	0.10	0.10	1665	+12.00	0.345±0.009
18:50:36.66107	+00:12:28.140	0.0009	0.020	22235	+14.53	1.026±0.011
18:50:36.6635	+00:12:28.21	0.003	0.05	22235	+18.75	0.244±0.007
18:50:36.6720	+00:12:28.41	0.017	0.17	22235	+20.22	0.110±0.012
18:50:36.66141	+00:12:28.191	0.0004	0.007	22235	+22.54	1.9844±0.0008
18:50:36.66040	+00:12:28.07	0.0013	0.03	22235	+25.07	0.690±0.010
18:50:36.66330	+00:12:28.147	0.0010	0.020	22235	+26.54	0.782±0.009

Notes. The parameters of the OH maser transition at 1665 MHz were reported by Beuther et al. (2019).

Table B.6: H_2O maser emission in our VLA observations of IRAS 18443−0231.

Maser coordinates		$\delta_{R.A.}$	δ_{dec}	Transition	V_{LSR}	S_ν
R.A.(J2000)	Dec(J2000)	(arcsec)	(arcsec)	(MHz)	(km s^{-1})	(Jy)
18:47:00.4421	−02:27:54.0	0.014	0.8	22235	−28.49	0.048±0.009
18:47:00.380	−02:27:53.7	0.03	0.5	22235	−17.11	0.055±0.012
18:47:00.40411	−02:27:52.552	0.0005	0.010	22235	−10.37	2.458±0.013
18:47:00.40336	−02:27:52.591	0.0003	0.007	22235	−9.32	3.875±0.014
18:47:00.4049	−02:27:52.54	0.005	0.09	22235	−6.37	0.234±0.012
18:47:00.40182	−02:27:52.587	0.0005	0.011	22235	−4.90	1.796±0.010
18:47:00.40120	−02:27:52.552	0.00016	0.004	22235	−3.42	9.826±0.018
18:47:00.4069	−02:27:52.56	0.003	0.06	22235	+0.16	0.315±0.009
18:47:00.4165	−02:27:52.03	0.009	0.23	22235	+1.42	0.098±0.012
18:47:00.4044	−02:27:52.60	0.006	0.12	22235	+2.47	0.14±0.08
18:47:00.4004	−02:27:52.56	0.003	0.05	22235	+5.05	0.390±0.012
18:47:00.40080	−02:27:52.472	0.0004	0.009	22235	+5.84	2.370±0.011
18:47:00.41120	−02:27:52.46	0.0017	0.04	22235	+7.74	0.543±0.011
18:47:00.41020	−02:27:52.53	0.0018	0.04	22235	+9.64	0.572±0.011
18:47:00.41332	−02:27:52.43	0.0015	0.03	22235	+11.54	0.653±0.010
18:47:00.40773	−02:27:52.58	0.0013	0.03	22235	+12.80	0.681±0.010
18:47:00.4208	−02:27:52.37	0.007	0.12	22235	+31.76	0.144±0.010
18:47:00.3810	−02:27:52.9	0.011	0.4	22235	+43.98	0.103±0.011
18:47:00.40251	−02:27:52.58	0.0017	0.04	22235	+48.61	0.488±0.010

Table B.7: H_2O and OH maser emission of IRAS 18213−1245A (from the literature).

Maser coordinates		$\delta_{R.A.}$	δ_{dec}	Transition	V_{LSR}	S_ν
R.A.(J2000)	Dec(J2000)	(arcsec)	(arcsec)	(MHz)	(km s^{-1})	(Jy)
18:24:09.73	−12:43:23.727	0.20	0.10	1665	+27.00	0.139±0.005
18:24:09.71	−12:43:23.96	8.7	1.36	22235	+23.60	3.70±0.05
18:24:09.71	−12:43:24.04	9.6	1.36	22235	+21.70	0.75±0.05

Notes. The H_2O masers were reported in HOPS (Walsh et al. 2014), and the OH masers in THOR (Beuther et al. 2019).

Table B.8: H_2O and OH masers in IRAS 18464−0140.

Maser coordinates		$\delta_{R.A.}$	δ_{dec}	Transition	V_{LSR}	S_ν
R.A.(J2000)	Dec(J2000)	(arcsec)	(arcsec)	(MHz)	(km s^{-1})	(Jy)
18:48:56.523	−01:36:43.32	0.20	0.20	1612	−28.10	1.749±0.021
18:48:58.62	−01:36:44.3	0.1	0.1	1665	−28.90	0.350±0.020
18:48:52.72	−01:36:44.3	0.1	0.1	1665	−29.45	0.500±0.010
18:48:56.52	−01:36:43.0	0.4	0.4	1667	−29.00	0.377±0.010
18:48:56.680580	−01:36:42.6796	0.00020	0.0025	22235	−37.89	34.85±0.17
18:48:56.6914	−01:36:42.72	0.014	0.13	22235	−28.68	1.01±0.20
18:48:56.65030	−01:36:43.040	0.0013	0.013	22235	−11.56	5.71±0.22
18:48:56.6462	−01:36:43.04	0.004	0.03	22235	−6.29	2.56±0.21

Notes. The 1612 and 1667 MHz OH maser emission were reported in THOR (Beuther et al. 2019), and the 1665 MHz OH maser in Forster & Caswell (1999). The H_2O maser emission was initially reported by Forster & Caswell (1999), but we reprocessed it completely, including normal calibration and self-calibration. The values given in this table correspond to those we obtained after this reprocessing.

Table B.9: Sources with discarded association in our ATCA/VLA observations.

Radio continuum emission				Maser emission			
Source name	Position RA, DEC (J2000)	Flux density[a] (mJy)	Frequency (GHz)	Source name	Position RA, DEC (J2000)	Flux density[b] (Jy)	Transition
RACS-DR1 J141249.8−69210	14:12:50.756 −69:21:03.56	48.6±0.7	2.1	IRAS 14086−6907	14:12:50.393 −69:21:09.75	5.61±0.04	OH 1612 MHz
IRAS 15559−5546	15:59:57.644 −55:55:33.24	69.3±1.8	2.1	IRAS 15557−5546	15:59:41.667 −55:54:51.21	1.49±0.06	OH 1612 MHz
IRAS 17385−2211	17:41:36.590 −22:13:03.90	0.68±0.09	2.1	IRAS 17388−2203	17:41:48.979 −22:05:17.03	2.56±0.05	OH 1612 MHz
		<1.0	1.5		17:41:48.963 −22:05:15.27	2.53±0.03	OH 1612 MHz
	17:41:36.610 −22:13:03.37	0.70±0.05	24			<42	H_2O 22 GHz
GPSR 020.590+0.425	18:27:07.018 −10:46:08.70	20.2±1.0	2.1	IRAS 18243−1048	18:27:08.273 −10:46:06.93	0.92±0.04	OH 1612 MHz
NGC 6644	18:32:34.682 −25:07:44.15	13.0±0.3	2.1	IRC −20491	18:32:07.675 −24:57:18.95	3.084±0.05	OH 1612 MHz
	18:32:34.687 −25:07:44.27	79.2±1.6	1.5		18:32:07.675 −24:57:18.95	3.09±0.04	OH 1612 MHz
	18:32:34.689 −25:07:44.18	78.0±0.4	24			<42	H_2O 22 GHz
K 3-33	19:22:26.694 +10:41:23.19	13.0±0.3	2.1	IRAS 19201+1040	19:22:29.168 +10:46:21.62	1.23±0.05	OH 1612 MHz
	19:22:26.669 +10:41:21.06	10.7±0.5	1.5		19:22:29.172 +10:46:21.00	2.56±0.05	OH 1612 MHz
	19:22:26.645 +10:41:20.30	15.34±0.08	24			<36	H_2O 22 GHz

Notes: [a] For sources in which radio continuum emission is not detected, we report the $3\,\sigma$ upper limit to the intensity (in mJy beam^{-1}). [b] For sources in which maser emission is not detected, we also report the $3\,\sigma$ upper limit, using the noise level (in mJy beam^{-1}), measured at the position and channel map with the $V_{\rm LSR}$ of the reported OH maser from single-dish observations.

Table B.10: Sources with undetected continuum and/or maser emission in our ATCA/VLA observations.

Target name	Date	Continuum[a]		Maser[b]	Telescope	Association[c]
		Frequency (GHz)	Flux density (mJy)	Flux density (mJy)		
IRAS 14079−6402	2021/10/19	2.1	1.81±0.16	<39	ATCA	UM
IRAS 16280−4008	2021/10/19	2.1	615.3±1.5	<87	ATCA	UM
IRAS 17180−2708	2021/10/20	2.1	265.0±0.3	<177	ATCA	UM
	2021/04/03	1.5	268.6±1.8	<117	VLA	UM
	2021/04/01	24	174.9±1.6	<27	VLA	UM
IRAS 17221−3038	2021/10/20	2.1	8.60±0.13	<114	ATCA	UM
IRAS 17253−2824	2021/10/20	2.1	<0.19	171±20	ATCA	UC
	2021/04/03	1.5	<2.0	224±14	VLA	UC
	2021/04/01	24	<0.04	<20.1	VLA	UC, UM
IRAS 17374−2700	2021/10/20	2.1	<0.18	<99	ATCA	UC, UM
	2021/04/03	1.5	<1.12	<72	VLA	UC, UM
	2021/04/01	24	<0.04	<24	VLA	UC, UM
IRAS 17403−2107	2021/10/20	2.1	11.26±0.16	<120	ATCA	UM
	2021/04/03	1.5	11.8±0.5	<114	VLA	UM
	2021/04/01	24	7.79±0.09	<33	VLA	UM
IRAS 18271−1014	2021/10/19	2.1	1.5±0.4	<33	ATCA	UM
	2021/04/03	1.5	<3	<60	VLA	UM
	2021/04/01	24	1.95±0.09	<18	VLA	UM
OH 25.646−0.003[d]	2021/03/25	24	<0.08	<36	VLA	UC, UM
IRAS 18551+0159	2021/04/03	1.5	143±5	<210	VLA	UM
	2021/03/25	24	189.6±0.4	<42	VLA	UM
IRAS 19123+1139	2021/10/19	2.1	29.5±1.0	<87	ATCA	UM
	2021/03/25	1.5	33±3	<237	VLA	UM
	2021/03/25	24	17.09±0.11	<36	VLA	UM
IRAS 19127+1717	2021/10/19	2.1	0.79±0.16	<60	ATCA	UM
	2021/03/25	1.5	2.2±0.4	<90	VLA	UM
	2021/03/25	24	5.94±0.05	<33	VLA	UM
IRAS 19508+2659	2021/03/25	24	<0.06	565±11	VLA	UC
IRAS 20266+3856	2021/04/03	1.5	<4	1336±180	VLA	UC
	2021/03/25	24	<0.06	<45	VLA	UC, UM

Notes. [a] For sources in which radio continuum emission is not detected, we report the $3\,\sigma$ upper limit to the intensity (in mJy beam^{-1}). [b] For sources in which maser emission is not detected, we also report the $3\,\sigma$ upper limit, using the noise level (in mJy beam^{-1}), measured at the position and channel map with the $V_{\rm LSR}$ of the reported OH maser from single-dish observations. [c] UC: undetected continuum emission. UM: undetected maser emission. [d] This object is a new OHPN candidate, but we have included it in this table because we did not detect any H_2O maser nor radio continuum emission in our VLA observations (see Appendix C.3.6).

Appendix C: Details on individual sources with association between maser and continuum emission

Appendix C.1: The OHPN IRAS 07027−7934: interferometric determination of maser positions in our observations

This source is the spectroscopically confirmed PN Vo 1 (Menzies & Wolstencroft 1990; Surendiranath 2002). OH observations with the 26-m Hartebeeshoek (beam=0.5°; Zijlstra et al. 1991) and the 64-m Parkes antennas (beam=13′; te Lintel Hekkert et al. 1991) show a symmetric double peak at 1612 MHz, with flux densities of $S_\nu \simeq 10$ Jy beam^{-1} and $V_{\rm LSR} \simeq -40$ and -47 km s^{-1}, as well as a single-peaked spectrum at 1667 MHz ($S_\nu \simeq 2$ Jy beam^{-1}, $V_{\rm LSR} \simeq -51$ km s^{-1}). Suárez et al. (2009) did not detect any H_2O maser emission in this source in spectra taken with the Parkes antenna (rms=0.22 Jy beam^{-1}). Despite the reported OH detections were carried out with single-dish antenna, Zijlstra et al. (1991) indicated that the Parkes beam was sufficiently small (13′) that the chance of confusion with other sources is negligible, given the high galactic latitude of IRAS 07027−7934. The LSR velocities of the reported OH maser components, ranging between −51 and −40 km s^{-1}, are blueshifted with respect to the systemic velocity of the source, traced by the CO peak (with $V_{\rm LSR} \simeq -27$ and -22 km s^{-1}; Loup et al. 1990; Zijlstra et al. 1991), and they are actually close to the blueshifted edge of the observed CO spectrum ($\simeq -40$ km s^{-1}). While double-peaked OH spectra in AGB stars have mean velocities coinciding with the stellar one, the blueshifted bias of maser emission seen in this source is a commonly observed trend in maser-emitting PNe (Uscanga et al. 2012).

In our interferometric ATCA observations, we detected maser emission at 1612 MHz (Fig. 2), but not at 1667 MHz (rms=13 mJy beam^{-1}). The LSR velocities of the observed maser components (Fig. 1; Table B.2) are similar to the 1612 MHz OH masers previously reported. However, the symmetric double peak spectrum of the 1612 MHz line has changed and is now clearly asymmetric, and has faded by a factor of ≃20. This fading correlates with the one of the maser at 1667 MHz, whose non-detection indicates a weakening of at least a factor of 50. The positional accuracy of our ATCA data does not allow us to determine the spatial distribution of the OH masers.

Our map of radio continuum emission at 2.1 GHz shows an unresolved source. Furthermore, the OH maser emission is located only at 0.″15 ± 0.″04 from the peak of the radio continuum, well within the beam of our ATCA observations (5.″3×3.″3). The positional accuracy in this match between maser and continuum emission improves by four orders of magnitude the one provided by previous single dish observations, which was determined by the size of the Parkes beam (13′). This positional coincidence further reinforces the classification of this source as an OHPN, previously proposed by Zijlstra et al. (1991) based on single-dish OH observations. Moreover, the masers arise from regions relatively close to the central star, as previously seen in other OHPNe (Christianto & Seaquist 1998; Miranda et al. 2001; Tafoya et al. 2009; Qiao et al. 2016a), and not from the faint extended structure observed in the Hα image, with an angular diameter of $\lesssim 15''$ (Zijlstra et al. 1991).

Vo 1 has been proposed to be a link between OH/IR stars and C-rich central stars (Zijlstra et al. 1991) since the observed OH masers could have been emitted only by an O-rich star at the AGB phase, and now Vo 1 harbors a [WC11] central star (Menzies & Wolstencroft 1990). Hence, this OH maser emission, the crystalline silicates and water ice (Cohen et al. 2002), suggest that Vo 1 is, in general, an O-rich nebula, while PAH emission arises from an elliptical shell surrounding the [WC11] central star over a region of ∼1.″0×0.″8 (García-Hernández et al. 2006).

Appendix C.2: New candidate maser-emitting PNe in our observations

Appendix C.2.1: IRAS 17487−1922

This source has been classified as a post-AGB star (Szczerba et al. 2007; Ramos-Larios et al. 2009). Single-peaked OH maser emission at 1612 MHz was reported at $V_{\rm LSR}$=−37.7 km s^{-1} based on 64-m Parkes observations (te Lintel Hekkert et al. 1991). We have detected this OH maser emission in our interferometric VLA and ATCA observations, and resolved it into several individual spectral features. In particular, in our ATCA observations, which have a better spectral resolution, we identified six emission features (Fig. 1, Table B.3). The positional accuracy of our ATCA/VLA data does not allow us to determine the spatial distribution of the OH masers. No H_2O masers were detected in previous observations with the 100-m Green Bank antenna (Gómez et al. 2015a), nor in our own VLA observations. The radio continuum emission is unresolved, and is reported here for the first time, as well as its association with OH masers. Hence, IRAS 17487−1922 is a new OHPN candidate.

Appendix C.2.2: IRAS 18019−2216

This source has been classified as an OHPN candidate by means of radio interferometric observations (Cala et al. 2022). Emission of H_2O masers was not detected in observations made in 2010 (rms=36 mJy beam^{-1}; Walsh et al. 2014). However, in our observations, made in 2021, we detected 22.235 GHz H_2O maser emission, where the brightest maser feature shows a S_ν=332 mJy beam^{-1} (Fig. 1 and Table B.4). Thus the H_2O masers seem to have emerged or presented significant variability between 2010 and 2021. Moreover, in IRAS 18019−2216, the OH and H_2O maser-emitting material are kinematically different, since the velocity range of the H_2O maser emission (from −10 to +8 km s^{-1}) falls outside that of the OH (from −38 to −29 km s^{-1}), as seen in other WFs (e.g., Boboltz & Marvel 2005; Yung et al. 2013; Vlemmings et al. 2014). Therefore, apart from being a H_2OPN and OHPN candidate, and taking into account this small spread of its H_2O maser emission, IRAS 18019−2216 is also a new 'low-velocity' WF (see Yung et al. 2013, for this classification).

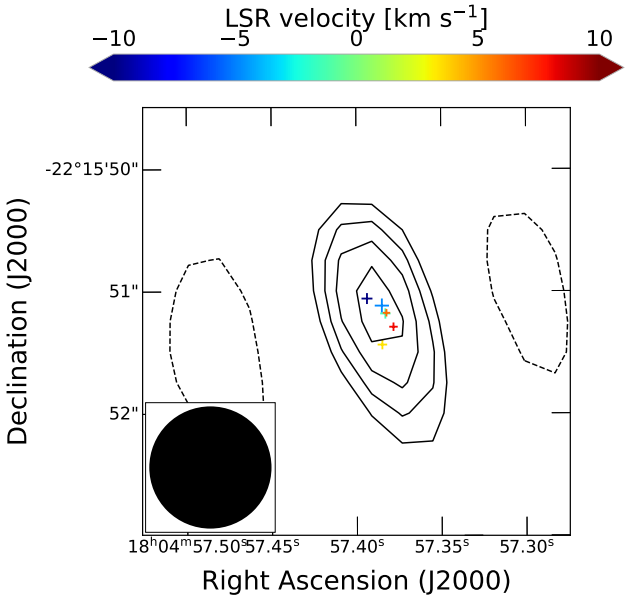

Fig. C.1: Radio continuum emission at 5.7 GHz of IRAS 18019−2216 from GLOSTAR. The contours are −3, 3, 4, 5, and 6 × 1σ (where σ = 90 μJy beam^{-1} is the rms of the map). The crosses are the positions of the H_2O masers, as shown in Fig. 2 (top left panel), assuming that the peak emission of the radio continuum emission at 22.22 GHz from our VLA observations lies at the same position as that of this map at 5.7 GHz. The color of the crosses represent the LSR velocity of the masers as indicated in the colorbar. The size of the crosses is proportional to the positional uncertainty of the masers. The beam is shown at the bottom left corner.

The spatial distribution of the H_2O masers in IRAS 18019−2216 (Fig. 2, top left) shows that the blueshifted and redshifted maser components occupy two different regions, (to the NE and SW, respectively), as expected in a bipolar jet. Fig. C.1 (left) shows the radio continuum map of IRAS 18019−2216 at 5.7 GHz obtained by GLOSTAR (Dzib et al. 2023) with the B configuration of the VLA. An elliptical Gaussian fit to the continuum emission indicates a deconvolved size of (≃3.″0±0.″53) × (0.″90±0.″03), and position angle ∼18±3°. This orientation is similar to the direction of the bipolar jet traced by the H_2O masers, as it can be seen in Fig. C.1, where we have assume that the peak emission of the radio continuum emission at 22.22 GHz from our VLA observations lies at the same position as that of this map at 5.7 GHz. This radio continuum emission at 22.22 GHz only shows an unresolved source.

Appendix C.2.3: IRAS 18443−0231

This optically obscured object has been classified as a PN by Cooper et al. (2013)[3] and Kanarek et al. (2015), based on its near-infrared spectrum with prominent emission lines and weak continuum emission, which can distinguish it from objects with similar infrared colors, such as H II regions or Wolf-Rayet stars. Although these works do not give any specific information that may allow us to discern whether the source is a late post-AGB

[3] Further characteristics of this object are available in http://rms.leeds.ac.uk/

star or a young PN, its SED (Fig. 3), peaking at ≃25 μm, strongly support that it is an evolved star.

An interesting feature in the infrared spectrum is that the ionized emission shows the recombination line of He I at 2.058 μm stronger than the Br γ emission (Cooper et al. 2013; Kanarek et al. 2015). This is consistent with the photoionized gas of young PNe that host a central star with $T_{\rm eff} \leq 40000$ K and present nebular electron densities larger than $\sim 10^4$ cm^{-3} (DePoy & Shields 1994; Lumsden et al. 2001a,b). However, using the 3MdB, we have checked that this emission line ratio can also be reproduced by shock-induced ionization (Cala et al., in preparation), and it is also seen in post-AGB stars showing shock-excited H_2 emission (Gledhill & Forde 2015). Hence, IRAS 18443−0231 seems to be a post-AGB star for which more research is needed to confirm its possible nature as a PN.

A spectrum of H_2O maser emission obtained with the 100 m Green Bank Telescope (Urquhart et al. 2011) shows a total velocity spread of maser components of 68 km s^{-1}, from $V_{\rm LSR} = -28$ to +40 km s^{-1}, indicating that this source could be a WF, as suggested by Ortega et al. (2024). However, given the presence of several H II regions in its neighborhood (Ortega et al. 2024), interferometric observations were necessary to discern whether all these maser components actually arise from IRAS 18443−0231. Actually, our VLA observations do interferometrically confirm the association between H_2O masers and the radio continuum. Moreover, our data also show H_2O maser components covering a wider velocity range than detected by Urquhart et al. (2011), with components between $V_{\rm LSR} = -28.5$ and +48.6 km s^{-1} (Fig. 1 and Table B.6). All these components, covering a total velocity spread of 77 km s^{-1} are spatially associated with the source, finally confirming IRAS 18443−0231 as a WF. We detected no OH maser emission in this source (rms ≃75 mJy beam^{-1}).

All H_2O maser components in this source are blueshifted with respect of the reported central velocity of the system, $V_{\rm LSR} = +110.3$ km s^{-1} (Urquhart et al. 2008). Thus, the detected maser emission would be tracing outflow motions of ≃ − 60 to −138 km s^{-1} along the line of sight. The systemic LSR velocity was estimated from a single-dish spectrum of the ^{13}CO(1-0) rotational line (Urquhart et al. 2008). We note, however, that those spectra show multiple spectral components, ranging from $V_{\rm LSR} = +50.4$ to +110.3 km s^{-1}. There is obvious interstellar confusion in this spectrum, which is normal for single-dish observations of molecular lines at the low galactic latitude of this source. The criterion used by Urquhart et al. (2008) to select the ^{13}CO component associated with the source was to choose the brightest one in the spectrum. This criterion seems reasonable for high-mass star-forming regions, which were the main targets for these authors, within the RMS survey. However, this criterion is not necessarily applicable to evolved objects, such as WFs. As an illustration, the CO(1-0) single-dish observations of ten WFs carried out by Rizzo et al. (2013) show contamination from multiple interstellar components in most of the spectra, and in no case the most intense component corresponds to the velocity of the source. The emission associated with these WFs, when detectable, is extremely weak. Anderson et al. (2011) also reported radio recombination line emission at 9 cm toward IRAS 18443−0231, at $V_{\rm LSR} = +63.4$ and +98.5 km s^{-1}, from observations with the Green Bank Telescope (beam size ≃82″). These lines most likely arise from the neighboring H II regions. Thus, we can conclude that there is no solid estimate of the systemic velocity of the source so far, and we tentatively assume the intermediate LSR velocity between the two most extreme H_2O maser components (≃ + 10 km s^{-1}) in the graphical representation of the maser velocities. If the systemic velocity of the source is confirmed to be close to this assumed one, then the weak CO emission around +120 km s^{-1} that Ortega et al. (2024) interpreted as tracing the redshifted lobe of molecular outflow from IRAS 18443−0231 is unlikely to be associated with the source.

Fig. 2 (bottom left) shows the spatial distribution of all the H_2O masers we identified, with respect to the radio continuum emission peak at 22.22 GHz, from our VLA observations. The H_2O masers trace a jet-like structure with an S-shaped morphology with a general north-south orientation on a larger scale. The maser components farther away from the center are the weakest ones, and they do not show a clear velocity distribution as expected in a jet (a trend of red- and blueshifted components separated on either side of the central source). However, the strongest innermost components (Fig. 2, bottom right) are arranged in a linear structure in the northeast (NE) to southwest (SW) direction, with a rough trend of more blueshifted components to the SW. The brightest maser components are blueshifted, and are located closer to this radio continuum emission peak. They seem to form a relatively dense cluster with a roughly circular or arc shape, suggesting the existence of bowshocks (as seen in, e.g., IRAS 18113−2503; Orosz et al. 2019), or the origin of a molecular jet as it emerges from the surrounding circumstellar material (as seen in, e.g., W43A; Tafoya et al. 2020).

Another outstanding characteristic of IRAS 18443−0231 is its spectral index, as mentioned in Section 5.5. Clearly negative spectral indices, characteristic of non-thermal radio emission, have been reported before in this source, with observations that indicate values $\alpha \simeq -1.15$ to $\alpha \simeq -0.36$ (e.g., Xu et al. 2006; Dzib et al. 2023). Some of these estimates should be taken with care, as the available information at radio frequencies of the source shows variability of a factor > 2 (Becker et al. 1994; Xu et al. 2006; Purcell et al. 2013; Medina et al. 2019; Dzib et al. 2023; Ortega et al. 2024). In this sense, the result of Xu et al. (2006) is more robust, as it was obtained with observations taken close in time.

Negative spectral indices, such as the one seen in IRAS 18443−0231, are characteristic of jets in which free electrons move in a magnetized environment. These jets are traced by the WF, and the derived spectral index $\alpha \simeq -0.42$ is similar to the spectral index of synchrotron jets of active galactic nuclei. Moreover, it has also been suggested that the powerful jets in this object can produce X- and γ-ray emission (Ortega et al. 2024), although the association of these high-energy emission with the source is still uncertain. Negative spectral index values have been reported in some WFs, such as the post-AGBs IRAS 15445−5449 and IRAS 18043−2116 (Pérez-Sánchez et al. 2013, 2017), and the nascent PN IRAS 15103−5754 (Suárez et al. 2015), as well as other post-AGB stars and PNe (Cerrigone et al. 2011, 2017). This group of non-thermal radio continuum emitters may be ideal sources for investigating the role of magnetic shaping of circumstellar structures in these evolutionary phases (e.g. García-Segura et al. 2020).

Figure C.2 shows the radio continuum emission of IRAS 18443−0231 at 24 GHz. It shows a compact, bright central component, plus some extended structure, with low-level extensions to the southwest, which are also observed in images at 3 and 5 GHz from VLASS and CORNISH, respectively (see Fig. 10 of Ortega et al. 2024). Archival VLA continuum map at 5.7 GHz shows an unresolved source at a beam size of 1.″2×0.″9. Similarly, Xu et al. (2006) reported an unresolved source (beam size 0.″9) at 15 GHz. We also show in Fig. C.2 the location of the H_2O masers, as presented in Fig. 2 (bottom panels). The

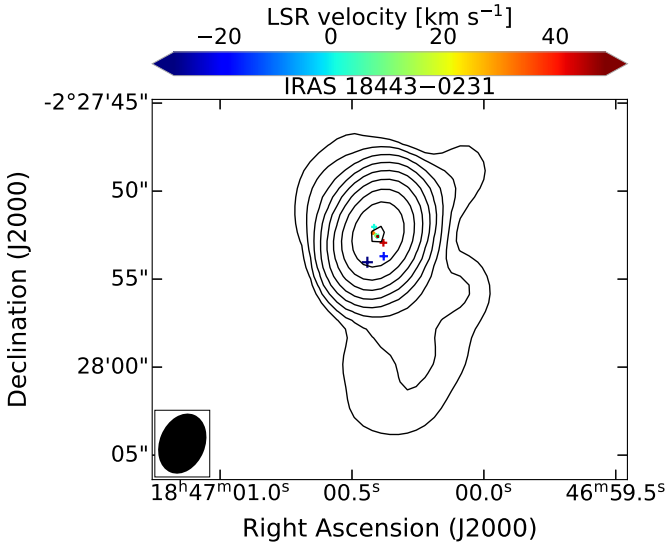

Fig. C.2: Contour map of the radio continuum emission of IRAS 18443−0231 at 24 GHz. The contours increment in steps of $3\sigma\times2^n$ starting from n=0 (σ= 0.23 mJy beam^{-1} is the rms of the map). The crosses are the positions of the H_2O masers, as shown in Fig. 2 (bottom panels). The color of the crosses represent the LSR velocity of the masers as indicated in the colorbar. The size of the crosses is proportional to the positional uncertainty of the masers. The beam is shown in the bottom left corner.

central linear structure of masers is located near the bright central non-thermal component of the ionized gas, although the weakest masers extend over a larger region and could be related with mass-loss along the direction of the extended continuum emission.

Appendix C.2.4: IRAS 18480+0008

The VLA THOR survey reported a single peak 1665 MHz maser feature at V_{LSR}=+12.0 km s^{-1} from this source (Beuther et al. 2019). VLA surveys of radio continuum have also reported this source with emission at 3 and 5 GHz (Medina et al. 2019; Gordon et al. 2021; Dzib et al. 2023). From these observations we report here for the first time this source as a OHPN candidate. Furthermore, our VLA observations show a match between H_2O masers and radio continuum emission at 22.22 GHz. The latter is unresolved in our data (beam ≃3″). Moreover, archival continuum data performed with the VLA in the B configuration at 5.7 GHz (beam ≃1″) also shows unresolved emission. The H_2O maser spectrum displays multiple spectral features emitted between V_{LSR}=+14 km s^{-1} and V_{LSR}=+28 km s^{-1} (Fig. 1 and Table B.5). The positions of the H_2O masers (Fig. 2, top right) trace a linear distribution from the northeast to the southwest direction, which is expected from either a collimated mass-loss event or a toroidal structure. Hence, IRAS 18480+0008 is a new H_2OPN and OHPN candidate, and could be a new WF. A confirmation of its nature as a WF would require further studies to determine the orientation of the nebula with respect to the water masers, or proper motion studies of the latter, to determine whether this maser emission actually traces a jet.

Appendix C.2.5: IRAS 19035+0801

This source has been classified as a candidate for PN based on its infrared colors and radio continuum emission (Van de Steene & Pottasch 1995; Irabor et al. 2018). Based on single-dish observations, Eder et al. (1988) reported single-peaked 1612 MHz OH maser emission at V_{LSR}=−80.2 km s^{-1}. We have also detected this maser emission at around −78 km s^{-1} in both ATCA and VLA observations and confirm that it has a positive positional coincidence with the source of radio continuum previously reported (see Fig. 1 and Table B.1). The positional accuracy of our data is not enough to determine the spatial distribution of the OH masers. We have not detected any H_2O maser emission. Hence, IRAS 19035+0801 is a new candidate for OHPN.

Appendix C.2.6: IRAS 19194+1548

This source was spectroscopically classified as a likely PN G50.4802+0.7058 (Sabin et al. 2014). OH maser emission at 6035 MHz has also been reported in this source, using ATCA interferometric observations (Avison et al. 2016). The 6035 MHz spectrum shows an asymmetric double peak at V_{LSR} of +48.12 and +48.22 km s^{-1} (see Table B.1). Data from the THOR survey report the presence of both OH maser emission at 1612 MHz (Beuther et al. 2019) and 1.5 GHz continuum emission (Wang et al. 2018) at the source position. These maser and continuum detections were reported separately, although they were obtained in simultaneous observations. The 1612 MHz OH maser emission shows only one emission feature at V_{LSR}=+43.5 km s^{-1}. The match between OH maser and radio continuum emission, as well as their association with this likely PN are reported here for the first time. In our VLA observations, we did not detect any 22.235 GHz H_2O maser emission.

In Figure C.3 we present an archival infrared image of IRAS 19194+1548 at 2.1 μm taken from the archive of the United Kingdom Infrared Telescope (UKIRT), which shows a point-symmetric bipolar nebula with a narrow waist. The position of the radio continuum emission (Wang et al. 2018) is near the center of the nebula, while the OH emission may be associated with the eastern lobe (relative positional accuracy of 0.″5). A Gaussian fit to our radio continuum map at 24 GHz indicates that the emission peak [RA(J2000)=19h21m40.421, DEC(J2000) +15d53m54.83s] lies at a position closer to the waist than to the lobes (see black point in Fig. C.3).

It should be noted that Akras et al. (2019) classified this object as a possible SySt, based on its SED, whose peak they reported to be at ≃4 μm. However, as shown in Fig. 3, our updated SED, including additional data, shows a peak between 30 and 70 μm, which is compatible with an obscured PN, rather than a SySt, as discussed in Sec. 5.1. In addition, an inspection of the spectrum shown by Sabin et al. (2014), suggests the presence of an emission line at 6830 Å that may be associated with the O VI Ramman-scattered line. However, this emission feature line is observed in both SySt and young PNe or may be a blending of several emission lines (see Akras et al. 2019, and references therein). On the other hand, the near-infrared spectrum obtained from the RMS survey[4] shows CO(3–1) emission at 2.31 μm (Cooper et al. 2013), which is observed in stars that have already entered the post-AGB phase (e.g. Hrivnak et al. 1994; Oudmaijer et al. 1995; Gledhill et al. 2011; Gledhill & Forde 2012). This emission is not expected in a SySt, where the main component is a red giant which only show CO absorption lines (Rayner et al. 2009). We also point out that, as mentioned before, this source has OH emission both at 1612 and 6032 MHz. The former is extremely rare in SySts (e.g., Norris et al. 1984;

[4] The spectra and further characteristics of this object are available at http://rms.leeds.ac.uk/

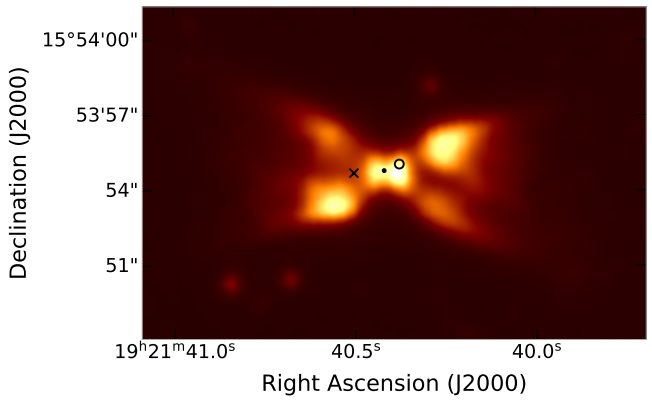

Fig. C.3: Near-infrared broadband emission at 2.1 μm of IRAS 19194+1548 by the UKIRT in logarithmic scale. The black empty circle and 'x' lie at the reported positions of the continuum emission peak at 1.5 GHz and 1612 MHz OH maser, respectively. The sizes are proportional to their relative positional accuracy. The black point lies at the position of the continuum emission peak at 24 GHz from our VLA observations. Its size is proportional to its positional uncertainty.

Seaquist et al. 1995), since the companion white dwarf ionizes the outer envelopes where these masers are produced, dissociating the OH molecules. Moreover, the 6035 MHz OH line has only been detected in young PNe (in Vy 2-2 and K 3-35; Jewell et al. 1985; Desmurs et al. 2002, 2010), but not in SySts.

In summary, there are some pieces of indirect evidence suggesting that this object could be a PN. However, here we report IRAS 19194+1548 as a new OHPN candidate (see also Márquez-Lugo et al. 2024), for which more research is needed to definitely confirm its nature as a PN.

Appendix C.3: New candidate maser-emitting PNe from the literature search

Appendix C.3.1: IRAS 16029−5055

This source, also called OH 331.158+00.781, has been classified as a post-AGB star due to its infrared colors and single peak OH spectrum at 1612 MHz, with $V_{\rm LSR}$ = −89.1 km s^{-1} (Sevenster et al. 1997). In the CORNISH South Survey, a weak radio continuum source has been reported, with a flux density of 3.20±0.39 mJy at 5.5 GHz (Irabor et al. 2023). No other radio continuum nor maser line emission has been reported on this source. We reported for the first time the match between the interferometric positions of this single-peak OH maser and the radio continuum emission. Moreover, the analysis presented in Sec. 5.4 of the archival *Spitzer* spectrum shown in Fig. 6 (top panel) allows us to strongly suggest the presence of photoionized gas. Hence, we report IRAS 16029−5055 as a new OHPN candidate, for which more observations are necessary before a final confirmation as bona fide OHPN (see Section 6).

Appendix C.3.2: IRAS 18213−1245A

Based on its infrared and radio continuum emission, this source has been classified as the PN candidate G018.5242+00.1519 (Urquhart et al. 2009; Irabor et al. 2018). Based on ATCA observations, Walsh et al. (2014) reported two H_2O maser features at $V_{\rm LSR}$ of ≃+21.7 km s^{-1} and ≃+23.6 km s^{-1} on this source. In addition, a wide 1665 MHz OH single peaked feature at $V_{\rm LSR}$=27 km s^{-1} covering a range of velocities of ∼15 km s^{-1} was reported by Beuther et al. (2019) in THOR, based on VLA observations. Although these maser and continuum data were not obtained simultaneously, their spatial locations are sufficiently close (distance ≃1″), and therefore, here we report the match between the interferometric positions of the PN candidate and these masers. Hence, IRAS 18213−1245A is a new H_2OPN and OHPN candidate.

Appendix C.3.3: IRAS 18464−0140

Based on its infrared and radio continuum emission, this source has been classified as the PN candidate G031.2131−00.1803 (Irabor et al. 2018; Medina et al. 2019). This classification as PN is supported by the non-detection of thermal ammonia emission (Anglada et al. 1996), which is more commonly detected in star-forming regions than in evolved stars (see Anglada et al. 1996; Wong et al. 2018). VLA observations in 1984 detected H_2O maser emission spread between $V_{\rm LSR}$ of −6.3 and −39.2 km s^{-1} and a peak emission of 20.2 Jy beam^{-1} at $V_{\rm LSR}$=−37.1 km s^{-1} (Forster & Caswell 1989, 1999). In addition, single emission peaks of OH maser emission at 1612, 1665, and 1667 MHz have been detected at $V_{\rm LSR}$ of −26.6 to −30.2 km s^{-1} based on VLA observations (Forster & Caswell 1989, 1999; Beuther et al. 2019). The 1665 MHz OH emission presents significant variability, with flux densities of ≃0.50 and 0.35 Jy (Table B.7) reported by reported by Forster & Caswell (1989), but it was not detected in THOR (rms=0.01 Jy beam^{-1}; Beuther et al. 2019). Based on the spatial coincidence of maser and continuum emission, we report IRAS 18464−0140 as a new H_2OPN and OHPN candidate.

Fig. C.4 shows a radio continuum map at 10 GHz of IRAS 18464−0140, which shows an elongated source with a deconvolved size of (344±14)×(53±36) mas^2 elongated at position angle 56±2°. We also show the location of the H_2O maser components from observations performed on 1984, and initially reported by Forster & Caswell (1999), which we reprocessed completely, including calibration and self-calibration. The increased signal-to-noise ratio, of a factor ∼2 in the maser emission, due to the self-calibration process, allowed us to detect two new components (at −28.68 and −6.29 km s^{-1}) not reported by Forster & Caswell (1999). The parameters of the detected maser components are shown in Table B.8. The blueshifted and redshifted maser clusters are separated ∼0.″7, and distributed along the same direction as the elongated continuum emission. This suggests that the masers are tracing a jet, which is characteristic of WFs (e.g. Suárez et al. 2008; Gómez et al. 2017). Hence, in addition to being a new H_2OPN and OHPN candidate, and considering this small spread of velocities of its H_2O maser emission, IRAS 18464−0140 is also a new 'low-velocity' WF (for this classification see Yung et al. 2013). We note that, while the association of maser and continuum emission, and their similar orientations are clear, it is not possible to exactly determine an accurate positional alignment between these two types of emission, since those data were not obtained simultaneously. It is likely that the masers actually lie at the tips of the bipolar structure traced by the continuum emission. Thus, new simultaneous H_2O maser and continuum observations are needed to accurately determine the location of the maser emission with respect to the nebula.

Appendix C.3.4: IRAS 18508+0047

Based on its infrared and radio continuum emission, this source has been classified as the PN candidate G033.9059−00.0436 (Urquhart et al. 2009; Irabor et al. 2018). A single 1612 MHz

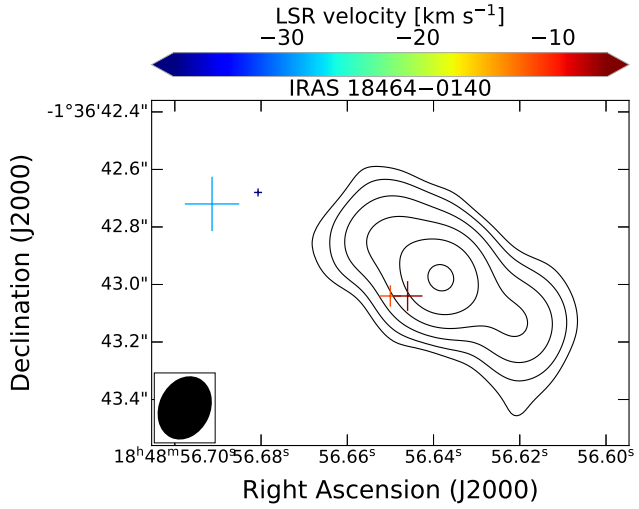

Fig. C.4: Contours of the radio continuum emission at 10 GHz of IRAS 18464−0140 from archival VLA data from observations performed on 2022. The contours increment in steps of $3\sigma\times2^n$ starting from n=0 ($\sigma = 31\,\mu$Jy beam^{-1}). The crosses are the positions of the H_2O masers obtained from our reprocessing of archival VLA data from observations performed on 1984. The color of the crosses represent the LSR velocity of the masers as indicated in the colorbar. The size of the crosses is proportional to the positional uncertainty of the masers.

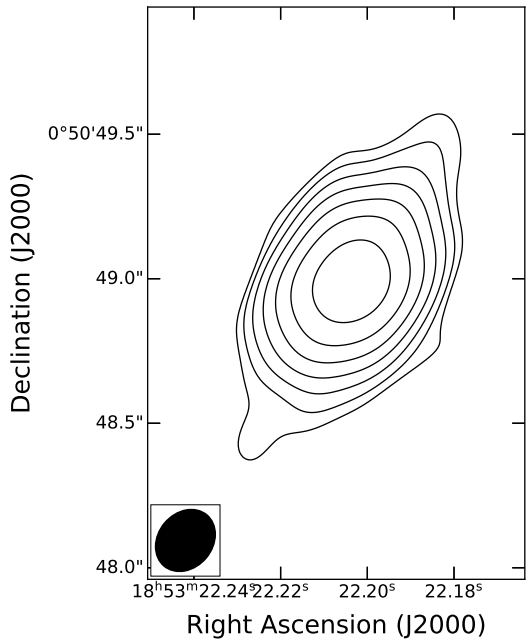

Fig. C.5: Contours of the radio continuum emission at 10 GHz of IRAS 18508+0047. The contours increment in steps of $3\sigma\times2^n$ starting from n=0 (where $\sigma = 44\,\mu$Jy beam^{-1} is the rms of the map). The filled ellipse is the synthesized beam of the radio continuum emission map.

OH maser feature at +76.5 km s^{-1} was reported at galactic position 33.906−0.044 by the THOR survey (Beuther et al. 2019). In this work, we report the match between the interferometric positions of the PN candidate and the OH maser emission (Table B.1). Hence, IRAS 18508+0047 is a new OHPN candidate. Fig. C.5 shows archival VLA continuum data from this source at 10 GHz. It originates from a strong compact source and weak extended emission in the northwest-southeast direction. A Gaussian fit indicates a deconvolved size of 284±3×200±2 mas^2, pa 147.9±1.2°.

Appendix C.3.5: IRAS 19176+1251

This source has been classified as the PN candidate G047.6884−00.3024, based on its infrared and radio continuum emission (Preite-Martinez 1988; Van de Steene & Pottasch 1995; Szczerba et al. 2007; Ramos-Larios et al. 2012; Irabor et al. 2018). Observations of H_2O masers have not detected emission on the source (rms=0.08 Jy beam^{-1}; Gómez et al. 2015a). Simultaneous observations of continuum and line emission detected both the 1.5 GHz radio continuum and the single peak 1720 MHz OH maser emission at −39.0 km s^{-1} (see Table B.1). These findings have been independently reported in the THOR survey for continuum and OH line emissions at the position of source G47.688−0.302 (Wang et al. 2018; Beuther et al. 2019). The analysis presented in Sec. 5.4 of the archival *Spitzer* spectrum shown in Fig. 6 (bottom right panel) is consistent with the presence of photoionized gas. Hence, we report IRAS 19176+1251 as a new OHPN candidate, for which more observational data are necessary before a final confirmation as bona fide OHPN (see Section 6).

To our knowledge, IRAS 19176+1251 is the first evolved low- to intermediate-mass star known to have detected OH maser emission at 1720 MHz, and without any association with other OH and H_2O maser, providing an excellent opportunity for investigation of the physical conditions for this OH maser transition in evolved stars. Although OH emission at 1720 MHz has been reported in other PNe (Miranda et al. 2001; Qiao et al. 2016a; Gómez et al. 2016), it was always found together with other OH maser transitions. The exclusive presence of OH masers at 1720 MHz is typical of shock waves of supernova remnants encountering interstellar molecular clouds (see Wardle & Yusef-Zadeh 2002), some star forming regions (Ogbodo et al. 2020), and in FU Ori-type outbursts (see Szabó et al. 2025, and references therein).

Appendix C.3.6: OH 025.646−00.003

A symmetric double-peaked maser spectrum at 1612 MHz has been reported from OH 025.646−00.003 in the THOR survey (Beuther et al. 2019). Radio continuum emission at 4.8 GHz has also been reported at this position (White et al. 2005). Here, the match between radio continuum and OH masers is reported for the first time. We did not detect H_2O maser nor radio continuum emission at 24 GHz from the source. Hence OH 025.646−00.003 is a new OHPN candidate.

Appendix D: Parameters of the shock and photoionization models

Taking into account the mid-infrared spectra of newly and previously identified objects (Fig. 6), we have used the fine-structure spectral lines of [Ne II], [Ne III], and [Ne V] seen at 12.81, 15.55, and 14.32 μm, respectively, to create diagnostic plots in the 3MdB (Morisset et al. 2015; Alarie & Morisset 2019) that represent shock ionization and photoionization models, which we describe below.

Appendix D.1: Shock models

We have used the 3MdB (Morisset et al. 2015; Alarie & Morisset 2019) to obtain the shock models of Sutherland & Dopita (2017), which follow the same grid definition as Allen et al. (2008), for a total of 15968 models. These models were then applied to generate the diagnostic diagram shown in Fig. 7 (left). The same models and parameters were used in Cala et al. (2024c), where a more detailed explanation can be found.

Appendix D.2: Photoionization models

We have used the 3MdB (Morisset et al. 2015; Alarie & Morisset 2019) to obtain the PN photoionization models of Delgado-Inglada et al. (2014). These models were computed using Cloudy v.17 (Ferland et al. 2017), resulting in a total of 68041 models. These models were then applied to generate the diagnostic diagram shown in Fig. 7 (right). The same models and parameters were used in Cala et al. (2024c), where a more detailed explanation can be found.

Appendix E: List of all confirmed water fountains

Table E.1 presents the list of all confirmed water fountain sources reported in the literature and newly identified in this work. For each object, its name, alternative designation, and velocity range of the H_2O masers are provided.

Table E.1: List of all confirmed water fountains.

Name	Alt. name	V_{range}[a] km s^{-1}	Reference[b]
IRAS 15103−5754	GLMP 405	70	1
IRAS 15445−5449	OH 326.5−0.4	90	2
IRAS 16342−3814	OH 344.1+5.8	260	3
IRAS 16552−3050	GLMP 498	170	4
IRAS 17291−2147	GLMP 498	70	5
IRAS 18019−2216	SCHB 281	20	This work
IRAS 18043−2116	OH 9.1−0.4	800	6, 7
IRAS 18113−2503	PM 1−221	500	8
IRAS 18139−1816	OH 12.8−0.9	50	9
IRAS 18286−0959	OH 21.80−0.13	200	10
IRAS 18443−0231	RFS 505	80	This work
IRAS 18450−0148	W43A	180	11
IRAS 18455+0448		40	12
IRAS 18460−0151	OH 31.0−0.2	310	13
IRAS 18464−0140	OH 31.21−0.18	30	This work
IRAS 18596+0315	OH 37.1−0.8	60	5
IRAS 19134+2131		100	14
IRAS 19190+1102	PM 1−298	100	15

Notes. [a] Velocity range of the H_2O masers to date. [b] Interferometric confirmation as WF and velocity range: 1. Gómez et al. (2015b). 2. Pérez-Sánchez et al. (2011). 3. Claussen et al. (2009). 4. Suárez et al. (2008). 5. Gómez et al. (2017). 6. Walsh et al. (2009) 7. Uscanga et al. (2023). 8. Gómez et al. (2011). 9. Boboltz & Marvel (2005). 10. Yung et al. (2011). 11. Imai et al. (2002). 12. Vlemmings et al. (2014). 13. Imai et al. (2013). 14. Imai et al. (2004). 15. Day et al. (2010).